Eulerian Method for Super-Cooled Large-Droplet Ice-Accretion on Aircraft Wings

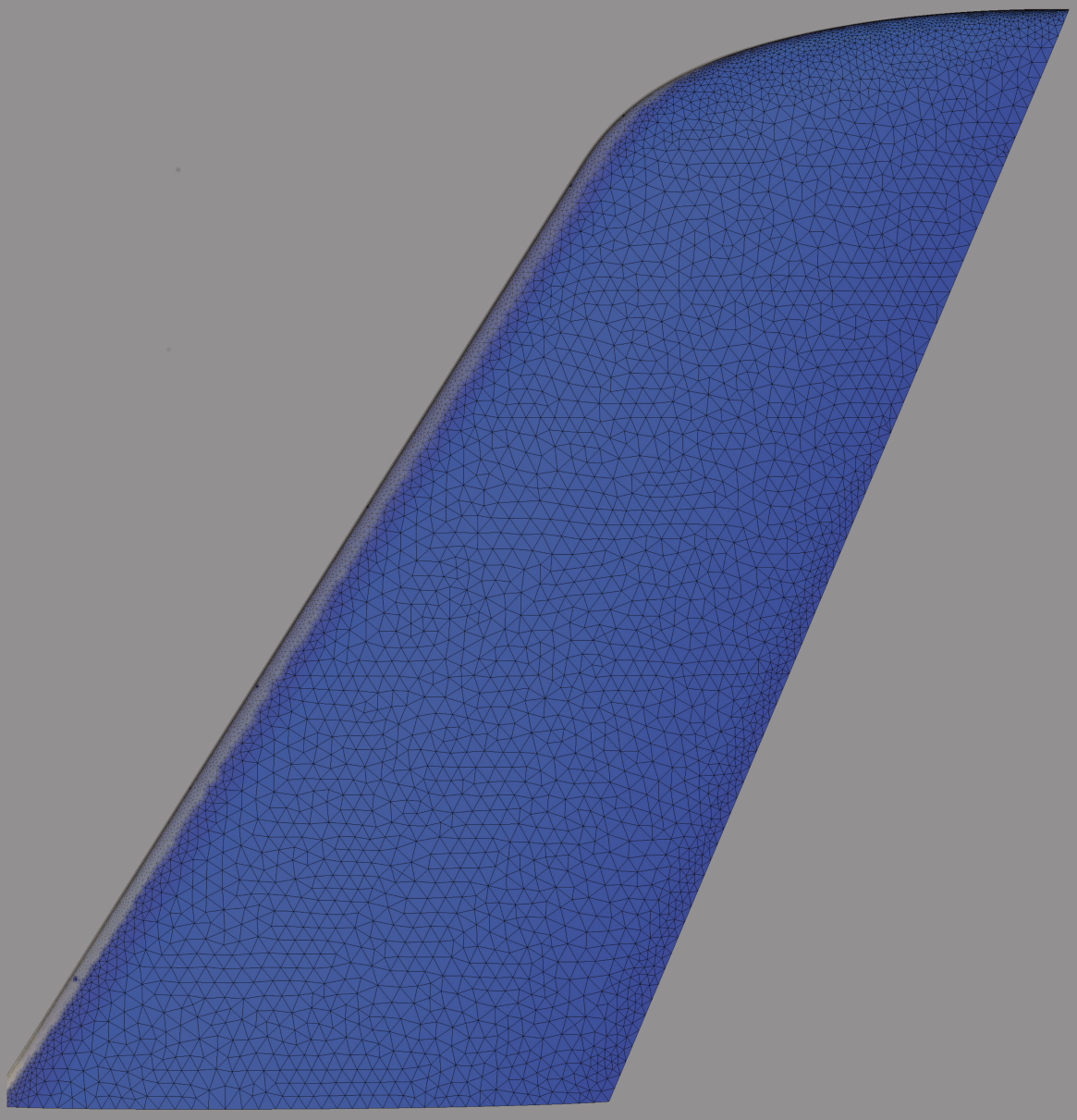

J.M. Hospers

EULERIAN METHOD FOR SUPER-COOLED LARGE-DROPLET ICE-ACCRETION ON AIRCRAFT WINGS

PROEFSCHRIFT

ter verkrijging van
de graad van doctor aan de Universiteit Twente,
op gezag van de rector magnificus,
prof.dr. H. Brinksma,
volgens besluit van het College voor Promoties
in het openbaar te verdedigen
op woensdag 27 november 2013 om 12.45 uur

door

Jacco Matthijs Hospers

geboren op 25 oktober 1983

te Almelo

Dit proefschrift is goedgekeurd door de promotor:
prof.dr.ir. H.W.M. Hoeijmakers
en assistent promotor:
dr.ir. E.T.A. van der Weide.

This thesis would not exist without the help of several people or institutions whom I would like to express my gratitude to here. First, thanks go out to my wife and daughter, who have been an inspiration and motivation for me. Furthermore, I would like to thank my other immediate family: my mom, dad, and sister. Without them I would have never come this far. On a more professional level I would like to express my gratitude to my professor Harry Hoeijmakers for allowing me to become part of the Engineering Fluid Dynamics group and be a part of this project in the first place. My colleagues whose work I have built upon and learned a lot from: Arjen Koop, Philip Kelleners and Jeroen Dillingh. Last but not least, I would like to thank the European Commission and in particular all partners involved with the FP7 EXTICE project for their collaboration and discussions. Without their work, experiments and data this thesis would not exist.

I wish you all the best and thank you for taking some of your time in reading my work.

ABSTRACT

Many research has been done to provide scientists and aviation engineers with tools to predict ice accretions on in flight aircraft. The ice accretion problem is often sudden, its effects can be dramatic, leading to aircraft accidents with possible loss of lives. Until now this field has been relatively steady. It has proven to be fairly easy to model ice accretions for clouds with droplets of relatively small droplet diameter (< 50 μm).

However, a recent trend is to investigate supercooled large droplets, with diameters ranging from 50 μm through 1000 μm or larger. These large droplets have been found to be more prominent in nature than previously thought. Ice accretions caused by these droplets have been identified as the likely cause for several aviation incidents during the last decade. Ice accretion by SLD are far more difficult to predict than those by smaller droplets. Development of ice accretion models for SLD has found renewed focus and was the central research theme in the European Commission FP7 EXTICE project. Much of the research in this thesis has its origins, or has been inspired by, this project.

A new SLD ice accretion method has been developed, incorporating: droplet size distributions, droplet deformation, droplet splashing, and droplet rebound. This method has been validated against experimental catching efficiencies and experimental ice accretions shapes. Furthermore, this method has been extended from a Lagrangian method for two-dimensional flow to an Eulerian method for three-dimensional flow. Validation results show an accuracy of droplet catching efficiencies within 10%. The ice accretion shapes are more difficult to accurately predict, but without a boundary layer film flow model the ice accretion thickness can also be predicted within approximately 10% accuracy.

CONTENTS

LIST OF TABLES

LIST OF FIGURES

NOMENCLATURE

Acronyms

CFD	computational fluid dynamics
CV	control volume
LWC	liquid water content
MVD	median volumetric diameter
SLD	supercooled large droplets

Subscripts

∞	free stream
a	air
d	droplet
in	incoming, primary droplet
out	outgoing, secondary droplet
s	surface
w	water

Symbols (Roman)

$\vec{D}$	drag force vector [N], see Eq. 2.2, page 12
$\vec{f}_D$	specific drag force [N/kg], see Eq. 4.5, page 39
$\vec{g}$	gravitational acceleration vector $\left[\mathrm{m/s^2}\right]$
$\vec{n}$	unit normal vector [−]
$\vec{U}$	velocity vector [m/s]
$\vec{x}$	position vector [m]
A	cross-sectional area $\left[\mathrm{m^2}\right]$
a	local speed of sound [m/s]
c	chord length [m]
C_D	drag coefficient [−], see Eq. 2.4, page 12
d	droplet diameter [m]
f	freezing fraction [−], see Eq. 2.8, page 16
K	Cossali splashing parameter [−], see Eq. 3.21, page 31
K_y	Yarin and Weiss splashing parameter [−], see Eq. 3.22, page 32
La	Laplace number [−], see Eq. 3.20, page 31

m mass [kg]
M Mach number based on the free-stream velocity [−], see Eq. 3.8, page 23
N_{bin} total number of droplet bins [−]
N_{cell} total number of grid-cells [−]
N_{conn} total number of grid-connectors [−]
Oh_d Ohnesorge number based on the relative droplet velocity [−], see Eq. 3.20, page 31
R_a average surface roughness [m]
R_{nd} non-dimensional surface roughness [−], see Eq. 3.25, page 33
Re Reynolds number based on the free-stream velocity [−], see Eq. 3.7, page 23
Re_d Reynolds number based on the relative droplet velocity [−], see Eq. 2.3, page 12
s airfoil coordinate [m]
T temperature [K]
t time [s]
u first component of the velocity vector [m/s]
v second component of the velocity vector [m/s]
w third component of the velocity vector [m/s]
We_d Weber number based on the relative droplet velocity [−], see Eq. 3.11, page 27
x first component of the position vector [m]
y second component of the position vector [m]
z third component of the position vector [m]

Symbols (Greek)

α volume fraction of water contained in droplets [−]
β catching efficiency [−], see Eq. 2.7, page 13 and Eq. 4.1, page 38
β_{total} total catching efficiency [−], see Eq. 6.1, page 67
μ local dynamic viscosity [Pa s]
ϕ mass loss coefficient [−], see Eq. 3.30, page 34 and Eq. 3.33, page 35
ρ density $\left[\mathrm{kg/m^3}\right]$
ρ_d droplet density $\left[\mathrm{kg_{water}/m^3_{air}}\right]$, see Eq. 4.2, page 38
σ Surface tension [Pa]
θ incident angle, with respect to the surface normal [°]

INTRODUCTION

1

> On October 31, 1994, at 1559 Central Standard Time, an Avions de Transport Regional, model 72-212 (ATR 72), registration number N401AM, leased to and operated by Simmons Airlines, Incorporated, and doing business as American Eagle flight 4184, crashed during a rapid descent after an uncommanded roll excursion. The airplane was in a holding pattern and was descending to a newly assigned altitude of 8,000 feet when the initial roll excursion occurred. The airplane was destroyed by impact forces; and the captain, first officer, 2 flight attendants and 64 passengers received fatal injuries. …
> The National Transportation Safety Board determines that the probable causes of this accident were the loss of control, attributed to a sudden and unexpected aileron hinge moment reversal that occurred after a ridge of ice accreted beyond the deice boots. …
>
> *NTSB AAR-96-01 , Aircraft Accident Report: In-Flight Icing Encounter and Loss of control, Simmons Airlines, d.b.a. American Eagle Flight 4184, Avions de Transport Regional (ATR), Model 72-212, N401AM Roselawn, Indiana, October 31, 1994*

THE ABOVE QUOTATION describes an example of an icing encounter, in this case unfortunately with fatal consequences. It is also one of the reasons for the current interest in research on icing on aircraft in flight. The cause of the severe icing in the fatal ATR 72 crash was the occurrence of so-called supercooled large droplets or *SLD*. The methods used by aircraft manufacturers are able to predict ice accretions occurring from *normal* icing conditions, with normal clouds containing droplets with a diameter up to 50 μm. However, SLD conditions, with droplets ranging to the millimeter scale, are much less understood. While the probability of encountering SLD icing conditions might not be as large as the probability of encountering "normal" icing conditions, the danger related to SLD icing greatly exceeds the danger of normal icing.

Figure 1.1: *Photograph of an ATR 72-212, American Eagle N440AM, same type as the aircraft from flight 4184*

1.1 ICE ACCRETION

When liquid water is carried upward in the atmosphere, due to thermal convection, clouds of water droplets are formed as shown in Fig 1.2. Depending on the altitude, temperatures inside these clouds can decrease below the freezing point (0 °C or 273.15 K). These droplets will not freeze unless there is a nucleus for the droplets to seed on, such as an existing ice crystal, a sand grain, or a dust particle. As such, clouds can contain *supercooled* droplets, droplets with a temperature below the freezing point. Typical temperatures can range from 0 °C down to −40 °C, depending on the altitude. When these droplets hit an object, such as an airplane wing, they will freeze almost instantly.

The ice accretion process involves several steps. When an aircraft flies through a cloud with supercooled droplets they impinge on the surface of the aircraft due to the forward velocity of the aircraft. The trajectory that a droplet follows, and therefore the location at which it will impact the surface, depends primarily on the droplet size; as the trajectory is determined mostly by the drag force on the droplet. Because the droplets

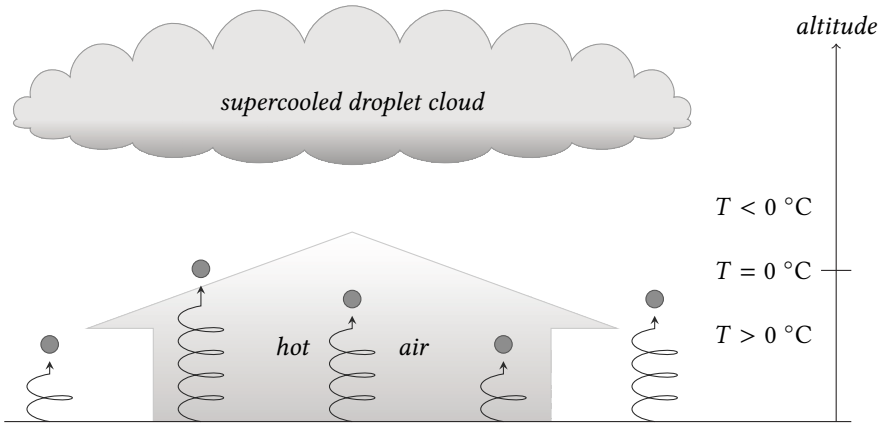

Figure 1.2: *Sketch of the birth of a supercooled cloud*

are supercooled, a mass of ice will form almost instantly at the moment the droplets contact the aircraft surface.

The size, shape, and location of the ice accretion that will form depends on:

- The environmental parameters, e.g., ambient air temperature, pressure, cloud liquid water content (LWC), relative humidity, and median volumetric diameter (MVD).
- The aircraft surface conditions, e.g., surface temperature, surface roughness, and surface tension at the air/water interface.
- The flow parameters, e.g., flight velocity, angle of attack, and icing time.

TYPES OF ICE ACCRETION 1.1.1

Two distinct types of ice accretion have been observed:

Rime-ice accretions A dry, opaque and milky-white ice deposit with a density lower than that of the water in the impinging droplets. It usually occurs at low airspeeds, low temperatures, and low LWC's. In

rime ice conditions the released latent heat of freezing is insufficient to raise the local temperature above the freezing point and all the water in the impinging droplet freezes fully upon impact. Generally, rime-ice accretions have a streamlined shape. This kind of icing is also called *freezing drizzle*.

Glaze-ice accretions A heavy coating of transparent ice spreading over the wing. This has a density close to that of the water in the impinging droplets. It usually develops at high airspeeds, temperatures closer to the freezing point, and high LWC's. In glaze-ice conditions, due to the relatively high amount of released latent heat of freezing, the temperature increases to 0 °C. Therefore, only part of the water in the droplets freezes upon impact, the rest of the water runs back along the airfoil surface. This run-back water often freezes further downstream on the airfoil surface. Generally, the resulting ice formations have an irregular, non-aerodynamic shape, which may jeopardize the aerodynamic characteristics of the airfoil section. This kind of icing is also called *freezing rain*.

1.1.2 ICE ACCRETION FEATURES

Several features are common in ice accretion shapes:

Roughness Ice that forms as a non-continuous distribution on the surface, usually at the onset of ice accretion. Roughness may grow into clear ice.

Feathers Similar to the roughness-feature, but these features extend further from the surface. Thought to be more prevalent in SLD conditions due to splashing and rebound of impinging droplets. Feathers may grow into clear ice or stream-wise ridges.

Clear ice Relatively smooth patches of ice, usually near the stagnation point.

Stream-wise ridges Typical rime icing shape, conforming to the surface. Stream-wise ridges may grow into horns.

Span-wise ridges Typical SLD feature. Formed by run-back water freezing downstream of anti-icing devices.

Horns Horns can grow just downstream of the stagnation point. It is common to encounter one or two horns, but more is possible. Horns can extend significantly in the direction normal to the surface.

For airplanes, ice accretions can cause severe problems because they disturb the aerodynamic characteristics of the airplane, e.g., an increase in drag due to increased surface roughness, or flow separation due to the horns. Ice accretions can also occur on engine intakes, causing dangerous situations when the ice detaches and is sucked into the engine.

low

Because of the inherent dangers of icing, airplanes have to be certified to be allowed to fly in icing conditions. For this certification a specification of the "normal" icing cloud has been formulated in the Federal Aviation Administrations (FAA) regulations: *FAA 14 CFR Part 25 Appendix C: Atmospheric Icing Conditions for Aircraft Certification.*

SUPERCOOLED LARGE DROPLETS 1.1.3

As a contrast to "normal" droplets, supercooled large droplets (SLD) are defined as droplets with a

- temperature below freezing ($T < 0$ °C or $T < 273.15$ K), and a
- diameter larger than normal droplets ($d > 50$ μm).

SLD encounters are rare. Wrongfully, they were attributed to conditions in alpine-climates, but SLD have been encountered in many other locations, including tropical-climates.

SLD are thought to be the main cause of the accident referred to in the introduction as well as several other aviation incidents. Because of their size SLD present specific problems because

- ice accretion occurs faster than for "normal" droplets.
- ice accretion occurs at different locations than where "normal" droplet ice accretion occurs. More water is transported downstream as runback water. This can cause ice accretions beyond the protection measures that are in place for "normal" icing.

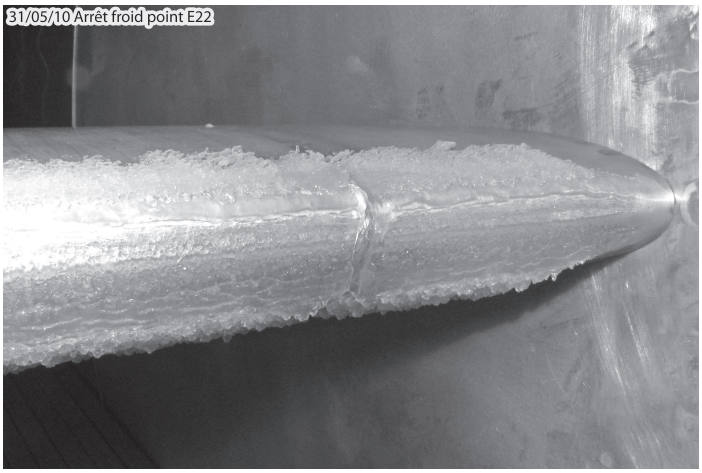

Photograph by DGA Essais Propulseurs

Figure 1.3: *Photograph of an icing wind-tunnel test showing an SLD-specific ice accretion, note the absence of horns*

- ice accretion is harder to predict than for "normal" droplets. SLD are more likely to splash, rebound, deform or break-up than "normal" droplets.

A typical example of SLD icing is shown in Fig. 1.3 and Fig. 1.4.

Droplets with sizes larger than 1 mm have been reported, e.g., in the EURICE project; which is much larger than the largest diameter (50 μm) prescribed in the *FAA 14 CFR Part 25 Appendix C* flight envelope.

The FAA is developing a new flight envelope, known as *FAA 14 CFR Part 25 Appendix O*, including SLD-conditions. The European Aviation and Space Agency (EASA) is developing similar regulations.

In preparation of these new regulations the industry wants to improve their understanding and predictive capabilities of SLD specific ice accretions. One such effort is the EXTICE project, a project funded from the European Union's seventh framework program (FP7). Much of the research presented in this thesis originates from this project. The present research focuses on the prediction of SLD trajectories and the corresponding distribution of water impinging on airfoils. Furthermore, the extension of this methodology to three-dimensional ice accretion simulation.

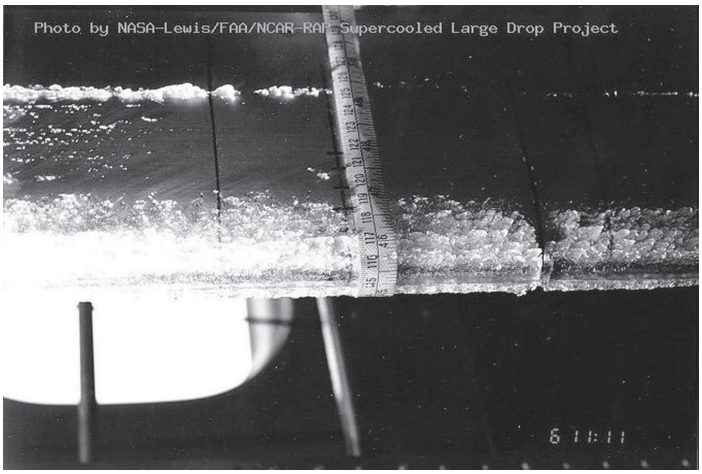

Photograph by NASA Lewis, now NASA Glenn

Figure 1.4: *Photograph of an icing wind-tunnel test showing an SLD-specific ice accretion, note the span-wise ridge*

ICE ACCRETION MODELING 1.2

Because of the impact of ice accretions, all aircraft manufacturers need and want to know the effects of *in-flight icing* on the aerodynamic characteristics of their aircraft. The reasons are threefold: they need to comply to certification demands regarding airworthiness with inoperative anti-icing devices, they want to design their aircraft such that the aircraft experiences minimal influence from in-flight icing, and they want to design their aircraft such that the need for anti-icing devices is minimal (in space, energy and cost). Combined with the many other demands for an aircraft, these design-requirements lead to a final aircraft design.

During the design-phase it is often impossible—on economical and practical grounds—to carry out in-flight ice accretion flight tests: a flying prototype must be available and the right atmospheric conditions must be found. Not to mention the possible dangers related to flying in icing conditions. Especially for SLD conditions this can be a daunting task! The only other options are:

1. wind-tunnel tests, this requires a scaled model of (part) of the aircraft and the availability of an icing wind-tunnel; and

2. numerical methods, this requires a sound mathematical model describing the physical processes involved in the formation of ice accretions and, of course, sufficient computing power.

Numerical methods are by far the most cost- and time-effective method of the two. However, it also requires the most (fundamental) knowledge of the physics involved in the entire ice accretion process.

Four separate stages of modeling can be identified:

Flow Model for Surrounding Air In order to predict the location of possible ice accretions the flow surrounding the aircraft must to be known. The geometry of the aircraft and the environmental conditions are used as input for this model. The model employs *computational fluid dynamics (CFD)* to obtain a realistic flow solution. The output from this model can be used to supply the droplet model with input.

Droplet Model Using the flow surrounding the aircraft, the cloud conditions, and the aircraft geometry as input; the droplet model must predict the distribution of impinging droplets on the aircraft surface, the so-called catching efficiency. Essentially, the equations of motion for the droplet have to be considered. The droplet physics involved for SLD droplets in the aircraft flow field are far more complicated than the physics for "normal" droplets. The output from this model can be used as input for the thermodynamic model.

Thermodynamic Model Using the flow near the surface and the impingement distribution from the above models, the thermodynamic model is able to predict the ice accretion using a mass and energy balance along the surface of the aircraft. The shape of the final ice accretion is determined by the mass and density of ice on the surface, caused by freezing of impinging water and of run-back water, if present. Water that does not freeze is used as input for the surface flow model.

Flow Model for the Surface Flow of Water Using the flow of air near the surface and the amount of water on the surface that does not

freeze, the surface flow model must predict how much water flows downstream along the aircraft surface. This can be a CFD-model based on film-dynamics, but often it is a simple empirical model. The run-back water is used as input for the above described thermodynamic model.

RESULTING ICE ACCRETION METHOD 1.2.1

The results of each of the above models depend on the other models, especially the surface flow and the thermodynamic model. Therefore, providing a solution method for these models is not evident. Usually the surface flow and thermodynamic model are combined into a single model. This leads to a sequential solution procedure. Some solution methods loop over these models several times, using the obtained ice accretion shape as a new (intermediate) aircraft geometry, i.e., as input for the air flow model).

OBJECTIVES OF PRESENT STUDY 1.3

This study aims at improving the existing numerical method for the prediction of ice-accretions to a more accurate method for SLD conditions. The resulting numerical method will provide predictions for ice-accretion shapes that are similar in shape and size to experimental results, in both two and three dimensions.

The outline of this study is as follows:

- A description of state-of-the-art numerical method.
- A detailed analysis of supercooled large droplets.
- A first improvement to the numerical method; solving a Eulerian droplet flow field. Including SLD specific effects, e.g., splashing and rebound.
- A second improvement of the numerical method; simulating three-dimensional ice accretions.
- Validation results of the introduced improvements.
- Concluding remarks.

PREVIOUS NUMERICAL METHODS 2

NOWADAYS, it is common practice in the aircraft manufacturing industry to apply computational methods for the prediction of ice accretions in two-dimensional flows. Studies to extend the two-dimensional ice growth methodology to three-dimensional flows are in progress at for example NASA Glenn as well as at CIRA and ONERA.

EXISTING ICE ACCRETION CODE 2.1

The 2DFOIL-ICE method [Jacobs et al., 2008, Dillingh and Hoeijmakers, 2003, 2004, Snellen, 1996, Snellen et al., 1997], developed at the University of Twente, predicts the growth of ice on 2D surfaces. It is based on a quasi-steady flow and ice growth model that takes into account all important mass and heat transfer processes that occur when supercooled water droplets strike an airfoil. The droplets either freeze immediately upon impact or freeze partly while the rest of the water runs back on the airfoil. The capabilities of the method have more recently been extended by the inclusion of a model for thermal ice protection systems [Dillingh and Hoeijmakers, 2003]. The use of this method, therefore, not only enables the assessment of potential icing hazards due to ice growth on unprotected surfaces; but also the design and appropriate placement of thermal ice protection systems. Aircraft icing is a threat during take-off and climb, during descent and landing, and in holding pattern flight; when high-lift devices of the multi-element airfoil are deployed. The geometric capability of the method has recently been extended to the case of multi-element airfoil sections [Jacobs et al., 2008].

LAGRANGIAN DROPLET MODELING 2.1.1

2DFOIL-ICE employs a so-called *Lagrangian* droplet tracking method. This means that droplets are followed individually from an initial release location

$\vec{x}_0 = (x_0, y_0, z_0)^T$. Along the droplet trajectory, a droplet velocity $\vec{U}_d = (u, v, w)^T$ can be determined by integration of the equation of motion for this droplet. If a suitable time-step Δt is chosen a new droplet position can be calculated.

The equation of motion for a droplet is usually taken to depend only on the droplet drag and on gravity. All other forces that may be acting on the droplet are ignored. As a result the equation of motion of the droplet can be expressed as:

$$m_d \frac{\mathrm{d}\vec{U}}{_d\mathrm{d}t} = \vec{D} + \vec{g} m_d, \tag{2.1}$$

with $\vec{g}$ the gravity and m_d the mass of a droplet. The drag force $\vec{D}$ is specified as:

$$\vec{D} = \tfrac{1}{2}\rho_a \left|\vec{U}_a - \vec{U}_d\right| \left(\vec{U}_a - \vec{U}_d\right) A_d C_D, \tag{2.2}$$

with ρ_a the density of the surrounding air. Furthermore, $\vec{U}_a$ and $\vec{U}_d$ are the air and droplet velocities, respectively. A_d is the cross-sectional area of the droplet. C_D is usually a function of the Reynolds number based on the relative droplet velocity, Re_d:

$$\mathrm{Re}_d \equiv \frac{\rho_a \left|\vec{U}_a - \vec{U}_d\right| d}{\mu_a}, \tag{2.3}$$

with d the droplet diameter and μ_a the dynamic viscosity of the surrounding air. In the current model C_D is derived from the expression due to Langmuir and Blodgett [1946]:

$$\frac{C_D \mathrm{Re}_d}{24} = 1 + 0.0197 \mathrm{Re}_d^{0.63} + 2.6 \cdot 10^{-4} \mathrm{Re}_d^{1.38}, \tag{2.4}$$

which is valid for $\mathrm{Re}_d < 1000$.

Integrating the equation of motion gives the droplet velocity

$$\vec{U}(t) = \int_{t'=0}^{t} \frac{\mathrm{d}\vec{U}}{\mathrm{d}t'}\,\mathrm{d}t' \approx \vec{U}_0 + \left.\frac{\mathrm{d}\vec{U}}{\mathrm{d}t'}\right|_{t'=t_0} \Delta t, \tag{2.5}$$

with $\Delta t = t - t_0$. The position of the droplet follows from

$$\vec{x}(t) = \int_{t'=0}^{t} \vec{U}(t')\,\mathrm{d}t' \approx \vec{x}_0 + \vec{U}_0 \Delta t. \tag{2.6}$$

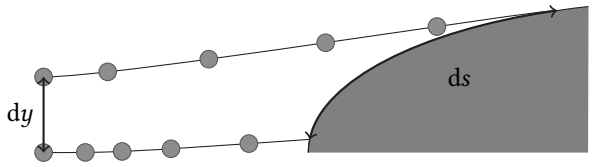

Figure 2.1: *Local catching efficiency for Lagrangian methods*

CATCHING EFFICIENCY

Using the calculated trajectories the *catching efficiency* can be determined. The catching efficiency is defined as the dimensionless mass of water impinging on the surface. For a Lagrangian method, this catching efficiency β is defined as:

$$\beta = \frac{\mathrm{d}y}{\mathrm{d}s}, \tag{2.7}$$

with dy the distance between two closely spaced trajectories at their release location and ds the distance along the surface between the corresponding two impact locations. A graphical example of this can be seen in Fig. 2.1.

A value of $\beta = 1$ implies that the distance between the two trajectories is the same on release and impact, i.e., the mass of water droplets contained between the two directories is exactly the same on the surface as at the start of the trajectory. A typical catching efficiency curve will show a peak value just below $\beta = 1$ around the stagnation point, decreasing away from the stagnation point in downstream direction where eventually it will decrease to zero. The points on the upper and lower surface closest to the stagnation point where $\beta = 0$ are called the impingement limits.

The catching efficiency is an important quantity for the prediction of ice accretions, since the ice accretion shape depends on the total amount as well as on the distribution of impinging water.

MESSINGER MODEL 2.1.2

Using the catching efficiency as one of the inputs, an ice accretion shape has to be calculated. Since the existence and shape of the ice is very much a local variable, a numerical scheme has to be conceived to calculate this amount of ice locally. One method that is often employed is the Messinger [1953] model. The Messinger approach can be described as follows:

- Divide the area along the surface into control volumes. Each control volume is limited by the surface on the bottom, the air on the top, and two neighboring control volumes; one upstream and one downstream. This means that a control volume may contains a layer of water, bounded on the bottom by either the ice layer or the airfoil surface, as illustrated in Fig. 2.2.

- **Iterate:**
  - Start using an initial guess temperature of 0 °C.
  - Calculate the mass balance for each of the control volumes on the surface.
  - Use the energy balance to calculate the temperature and a freezing fraction.
  - Repeat until the temperature and freezing fraction reach convergence.

Using this method it is possible to find an equilibrium state for each of the control volumes. The details of this method will be explained in the following sections.

MASS BALANCE

The mass balance is determined by the difference between the mass entering the control volume and the mass leaving the control volume.

Incoming mass: Sources of mass for each control volume.

- mass of impinging droplets
- mass of runback water from upstream control volumes

Outgoing mass: Sources of mass loss for each control volume.

- mass of water that freezes, determined by the energy balance
- mass of runback water to downstream control volumes
- mass of water evaporating from the surface

The outgoing mass flows are dependent on the resulting mass of ice, which is determined by the thermodynamic balance. These mass flows are illustrated in Fig. 2.2(a).

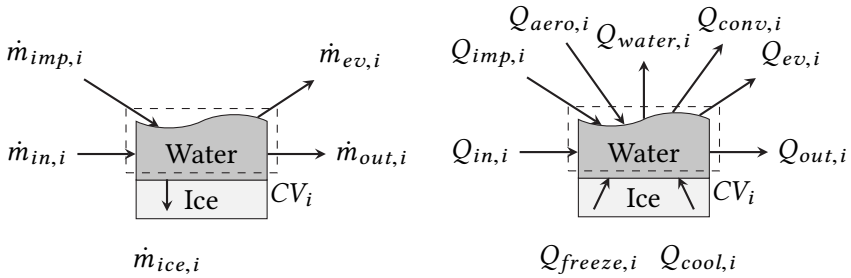

(a) *Mass flows* ***(b)*** *Energy flows*

Figure 2.2: *Messinger control volume, 2D*

THERMODYNAMIC BALANCE

The thermodynamic balance determines if, and how much, water freezes on the surface. A balance has to be found between the incoming and outgoing energy of a control volume.

Incoming energy: Sources of energy for each control volume.

- kinetic energy of impinging droplets
- enthalpy of impinging droplets
- enthalpy of runback water from upstream control volumes

Outgoing energy: Sources of energy loss for each control volume.

- latent heat of freezing water
- latent heat of evaporating water
- enthalpy of remaining water film
- enthalpy of runback water to downstream control volumes

All of these terms contribute to the energy balance, depending on the temperature of the surface T_s and on the surrounding air T_e. These energy flows are illustrated in Fig. 2.2(b).

ITERATION PROCEDURE

To satisfy the mass and energy balance an iterative procedure is used. The unknown parameters are the leaving mass, the temperature, and the so-called freezing fraction. The iterative procedure starts at the stagnation point (2D) or stagnation line (3D), where there is no runback water from upstream control volumes. For such a control volume the only entering mass is the impinging droplet mass.

As an initial guess, the temperature for each control volume is chosen as 273.15 K, the freezing point of water. At this temperature it is possible to have a mixture of ice and water: the freezing fraction, f, needs to be determined:

$$f \equiv \frac{\text{freezing mass}}{\text{incoming mass}}. \tag{2.8}$$

The next step in the iteration procedure is determined by three ranges for the freezing fraction:

$$\begin{aligned} f < 0: &\quad T_{s,1} = T_{s,0} - \Delta T_s, \text{ no water} \rightarrow \text{ice} \\ 0 \leq f \leq 1: &\quad T_s \text{ is correct, some water} \rightarrow \text{ice} \\ f > 1: &\quad T_{s,1} = T_{s,0} + \Delta T_s, \text{ all water} \rightarrow \text{ice} \end{aligned} \tag{2.9}$$

If $0 \leq f \leq 1$, the mass of water not turning into ice is the amount of runback water. The iteration process is illustrated in Fig. 2.3.

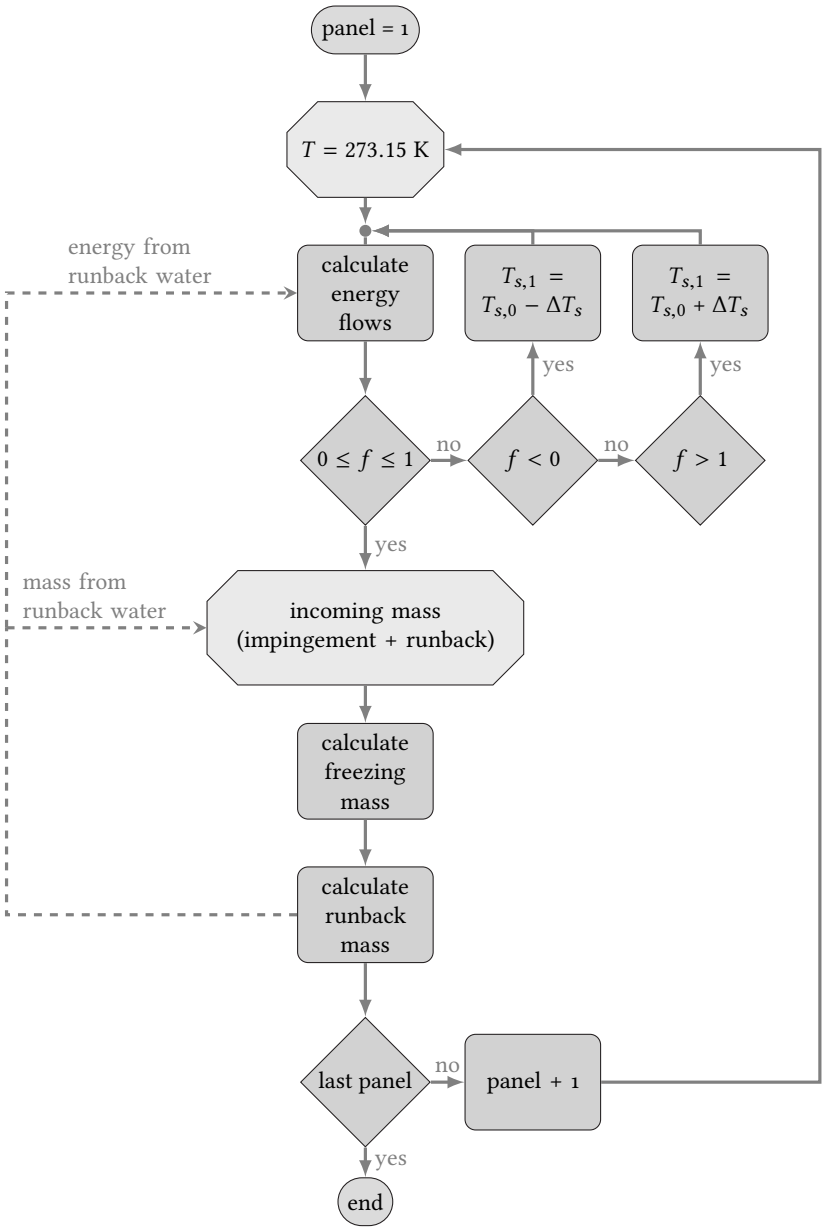

Figure 2.3: *Flow chart of the iteration procedure used with the Messinger method*

3 SUPERCOOLED LARGE DROPLETS

THE MOST IMPORTANT REASON why SLD ice accretions differ from normal ice accretions is the droplet size and the specific effects that are encountered when flying in conditions with these droplets. The SLD droplet effects are:

deformation Shear forces make SLD more likely to deform then smaller droplets.

breakup Larger shear forces may lead to breakup of SLD's.

splashing SLD's are more likely to splash upon impact with a surface.

rebound Similar to splash, but the entire droplet is deflected instead of a splash event, creating multiple droplets.

These effects make it more difficult to predict SLD droplet trajectories, which is necessary to carefully predict the resulting ice accretion shape.

3.1 EFFECT ON EXISTING MODELS

The aforementioned SLD specific effects have a severe implication on the existing ice accretion models.

The droplet deformation effect can be taken into account by modifying the relation for the drag of the droplets, as shown in section 3.2.1. However, the resulting relation is not a straightforward one, since it will depend on the Reynolds number, the Weber number, or on a combination of these.

Droplet breakup is already a far more challenging aspect. There are relations readily available from literature, see section 3.2.2, to determine the moment and time of breakup; but the difficulty lies in the droplets that are formed after the breakup event. These *secondary droplets* will have a smaller diameter than the primary droplet and thus will have different characteristic properties, for drag or splashing events. Furthermore, every

breakup event will result in secondary droplets with a different diameter. This means that multiple droplet sizes will have to be tracked.

According to Wright and Potapczuk [2004], splashing is of primary influence on the resulting SLD ice accretions, it is also one of the most challenging effects to accurately model. The assumption for non SLD droplets is that, upon contact, they always impinge on a surface. Splashing implies that this is no longer true: a droplet may splash, resulting in the re-injection of several secondary droplets, with a smaller diameter, into the flow around the surface; but also in the possible deposition of part of the original droplet on the surface. There are some splashing models available in literature, see section 3.2.3, but their implementation is not straightforward. The location on the surface where the secondary droplets are formed needs to be tracked to correctly account for the mass lost by secondary droplets being entrained in the flow. This loss of mass is indicated by the mass loss coefficient, ϕ. The mass loss coefficient can range from $\phi = 0$ (no mass loss, all mass deposits on the surface) to $\phi = 1$ (no mass deposits on the surface). Again, as with the breakup effect, multiple droplet sizes will have to be tracked.

The rebound effect is very similar to the splashing effect. However, now the resulting secondary droplet is of the same diameter as the primary droplet. Furthermore, there is no deposition of mass on the surface: $\phi = 1$. This results in a simpler numerical implementation, shown in section 3.2.4.

Finally, both splashing and rebound are influenced by the existence of a liquid film layer on the airfoil surface. This film surface is modeled by a constant surface roughness influence in the heat transfer equations. The film is not modeled as a dynamic fluid layer. However, due to the larger mass of incoming water, larger water film thickness may occur, and liquid film modeling may become necessary, as has been investigated by Norde [2013].

3.1.1 DROPLET TRAJECTORIES

To be certain that the aforementioned effects are the major effects that play a role in the simulation of SLD droplet trajectories, a study into the forces acting on these droplets has been performed. In the work of van Eijkeren and Hoeijmakers [2010] a comprehensive analysis of the available models for the forces acting on droplets surrounded by a fluid flow was performed.

Using these models, the impact of each of the separate forces has been assessed.

For normal droplets, it is common to assume that all forces besides drag, gravity and buoyancy can be ignored. To assess if this is a valid assumption for the larger SLD's an analysis of two different sets of trajectories has been performed. One set of trajectories has been calculated using the conventional assumption (only drag, gravity and buoyancy) and the other set was calculated using a number of additional forces. The set of possibly relevant forces consists of:

- drag,
- gravity,
- buoyancy,
- Basset history force, and
- virtual mass force.

The complete force on a droplet contains even more force-terms, some of which are unknown. There are some lift terms, e.g., the Saffman lift force, but these force terms depend on rotation of the droplet or the containing fluid. Since for most calculations the potential-flow assumption is used, which implies that rotation of the flow field is negligible, these rotational lift terms are ignored.

DRAG FORCE

The drag force is accounted for using Eq. 2.2 from section 2.1.1, repeated here:

$$\vec{D} = \tfrac{1}{2}\rho_a \left|\vec{U}_a - \vec{U}_d\right| \left(\vec{U}_a - \vec{U}_d\right) A_d C_D.$$

GRAVITY FORCE

In most conventional models the gravity is combined with at least part of the buoyancy force. For this study the two have been accounted for as individual force terms. The gravity force consists only of the force acting on the droplet by gravitational acceleration:

$$\vec{f}_g = \rho_w V_d \vec{g}; \tag{3.1}$$

where ρ_w is the density of water, V_d the volume of a droplet, and $\vec{g}$ the gravitational acceleration vector.

BUOYANCY FORCE

The buoyancy force is caused by a pressure gradient. In most common methods, only the constant pressure gradient caused by the constant gravity field is taken into account, resulting in

$$\vec{f_b} = -\rho_a V_d \vec{g}, \tag{3.2}$$

where ρ_a is the density of the surrounding fluid (air). However, for the present analysis the pressure gradient also takes into account the local pressure gradient, $\vec{\nabla} p$, induced by the flow field:

$$\vec{f_b} = -V_d \vec{\nabla} p. \tag{3.3}$$

BASSET HISTORY FORCE

Perhaps the most important question is whether or not the Basset history force has to be accounted for. This term is based on the relative speed at which the boundary layer on the droplet surface adapts to changes in the surrounding flow. Calculation of this term is particularly complicated because it involves a time-integration over the path of the droplet, i.e., accounting for its history:

$$\vec{f_B} = -3d\mu_a \pi \int_{-\infty}^{t} K\left(t-\tau,\tau\right) \frac{\mathrm{d}\left(\vec{U}-\vec{U_d}\right)}{\mathrm{d}t}\,\mathrm{d}\tau. \tag{3.4}$$

where the kernel K has been chosen as the kernel for non-creeping flow conditions from Mei et al. [1991]:

$$K\left(t-\tau,\tau\right) = \left[\left(\frac{4\pi\left(t-\tau\right)}{\tau_d}\right)^{0.2} + \left(\frac{\pi\left(t-\tau\right)^2}{f_H^3 \tau_d^2}\mathrm{Re}_d^3\right)^{0.4}\right]^{-2.5}, \tag{3.5}$$

with the droplet relaxation time $\tau_d = \frac{\rho_a d^2}{\mu_a}$ and $f_H = 0.75 + 0.2\mathrm{Re}_d$.

VIRTUAL MASS FORCE

The virtual mass force is based on the acceleration of the air surrounding the droplets. Accelerating a droplet means that the air surrounding it has to accelerate as well. The virtual mass force therefore depends on the relative acceleration:

$$\vec{f}_{vm} = \frac{1}{2}\rho_a V_d \frac{\mathrm{d}\left(\vec{U} - \vec{U}_d\right)}{\mathrm{d}t}. \tag{3.6}$$

RESULTS

The two sets of droplet forces were used to perform calculations for two droplet sizes. The droplet sizes chosen are the minimum and maximum droplet diameters from the 10-bin droplet size distribution determined in an impingement experiment performed by Papadakis et al. [2007], also used in the validation of the complete model in chapter 6: 16 μm and 1046 μm, respectively. The considered configuration is a NACA 23012 airfoil of 0.9144 m at 2.5° angle of attack. The free-stream velocity $\vec{U}_\infty = 78.23$ m/s. With the Reynolds number as

$$\mathrm{Re} \equiv \frac{\rho_\infty \vec{U}_\infty c}{\mu} = 4.4 \cdot 10^4 \tag{3.7}$$

and the Mach number as

$$\mathrm{M} \equiv \frac{\vec{U}_\infty}{a} = 0.23, \tag{3.8}$$

where c is the airfoil chord length and a the free-stream speed of sound.

For this configuration the impingement limits were determined and approximately 100 droplet trajectories were calculated within these limits. The results are shown in Fig. 3.1.

For each of the force-components the trajectory with the maximum force magnitude was determined, and the identification number of this trajectory was stored. The trajectories corresponding to unique trajectory identification numbers were plotted. This results in two or three different trajectories for each set of calculations, which indicates that most droplet force components have a maximum force in the same trajectory. Furthermore, the droplet trajectories that are *not* the same are geometrically very close to each other resulting in very similar trajectory plots.

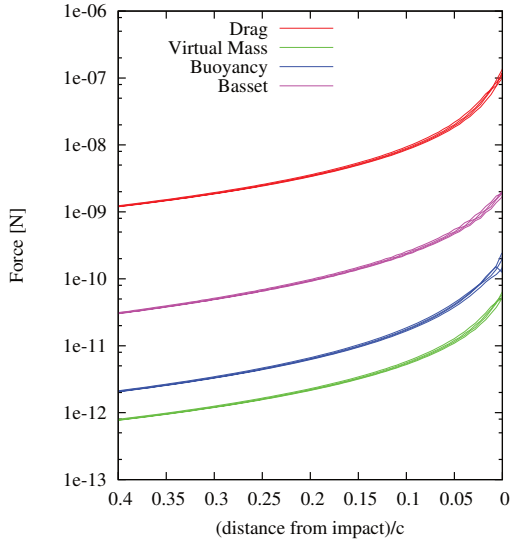

(a) *Droplet diameter, $d = 16$ µm*

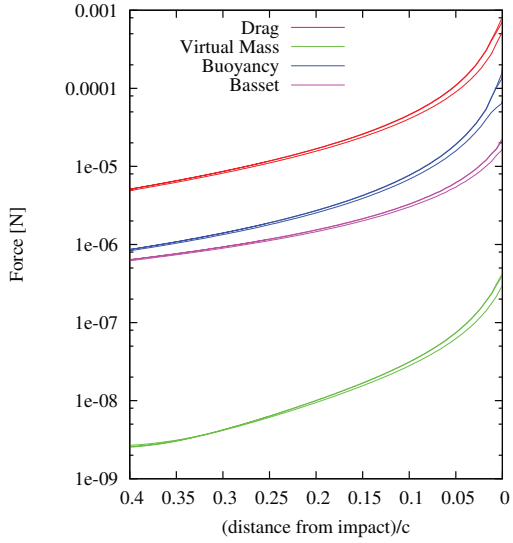

(b) *Droplet diameter, $d = 1046$ µm*

Figure 3.1: *Magnitude of force components along droplet trajectories, only trajectories for which one of the components has a maximum value are shown*

Based on the resulting trajectories it can be concluded that:

- For both droplet sizes the drag force is the dominant force, although the order of magnitude is almost four times larger for the larger droplets than it is for the smaller droplets.
- For the smaller droplets (Fig. 3.1(a)) the second most dominant force is the history force. However, this force component is already more than one order of magnitude smaller than the drag force.
- For the larger droplets (Fig. 3.1(b)) the buoyancy force becomes more important than the history force, the history force term is, similar to the secondary force term for the smaller droplets, around one order of magnitude smaller than the dominant drag force.

The calculation of the history force term is very time-consuming since it involves integration over the entire time-domain up to the considered time. Furthermore, the history force acts as in the same direction as the drag force term. When ignoring the history force, part of the ignored effects are compensated by an increase in the drag force. This gives reason to continue with the generally accepted method of including only drag, buoyancy and gravity in the calculation of droplet trajectories. It would be very time consuming to include the history force in the numerical model, while the increase in accuracy of the resulting droplet trajectories is minimal.

AVAILABLE SLD MODELS 3.2

For each of the effects listed in section 1.1.3 there are models available from literature. The most appropriate model for each SLD effect is described below.

DEFORMATION 3.2.1

One of the effects that becomes noticeable for larger droplets is due to droplet deformation. Larger shear forces in the flow can cause droplets to deform. This means that the assumption that a droplet behaves as a solid sphere (Eq. 2.4) is no longer valid.

Droplet deformation may lead to droplet breakup. Droplets that are deformed or stretched beyond a certain limit will eventually breakup. Therefore, similar relations apply to droplet deformation and droplet breakup.

FEO

One attempt to improve the trajectory calculations due to the deformation of droplets is by Feo and Jarillo [2008] as part of the EXTICE project. In this work the droplet drag coefficient is determined from droplet velocity while moving towards an airfoil. Feo used a high speed camera to with double exposure to capture droplet sizes and motion. These drag coefficients are then compared to the drag coefficients for spheres.

Using this data, a linear approximation of the drag coefficient as a function of the local Reynolds number is proposed. Feo's data suggests that for low droplet Reynolds number the spherical model is valid. For a droplet Reynolds number larger than $\mathrm{Re}_d > 345$, the spherical droplet drag coefficient is modified. Data is not available for $\mathrm{Re}_d > 720$, leading to the following linear relations [De Gennaro, 2009, Mingione, 2012]:

$$\frac{C_D \mathrm{Re}_d}{24} = \begin{cases} -0.00355\mathrm{Re}_d + 3.760 : & 345 < \mathrm{Re}_d \leq 385 \\ -0.00517\mathrm{Re}_d + 4.782 : & 385 < \mathrm{Re}_d \leq 442 \\ -0.00255\mathrm{Re}_d + 3.425 : & 442 < \mathrm{Re}_d \leq 475 \\ 0.0318\mathrm{Re}_d - 12.903 : & 475 < \mathrm{Re}_d \leq 518 \\ 0.00333\mathrm{Re}_d - 0.313 : & 518 < \mathrm{Re}_d \leq 630 \\ -0.00325\mathrm{Re}_d + 2.221 : & 630 < \mathrm{Re}_d < 720 \end{cases} . \tag{3.9}$$

Note that there is no direct time dependence in this relation, while deformation—like breakup—is very much a time dependent process. Note that Eq. 3.9 is valid only for water droplets, no droplet properties are included in this model.

TAB-MODEL

The Taylor analogy breakup (TAB) model is, as it's name implies, a breakup model (see section 3.2.2); it uses droplet deformation to estimate when a droplet will breakup, but it can also be used to modify the droplet drag coefficient. One such model is, according to Tan et al. [2005], used in

FLUENT©; it uses the droplet deformation described in the TAB breakup model, Eq. 3.15, to modify the droplet drag coefficient

$$C_D = C_{D,sphere}\left(1 + 2.632y\right), \tag{3.10}$$

where y is the non-dimensional deformation of a droplet, as described in Eq. 3.18.

BREAKUP 3.2.2

If the stresses on a droplet are large enough (larger than the stresses needed to deform a droplet), or the deformation persists long enough; the droplet might breakup into smaller droplets. A review on different breakup models has been performed by Tan et al. [2005].

Breakup is a cascading process; droplets will continue to breakup, under the stresses imposed by the flow on the droplet, until a certain critical diameter is reached. Droplets with a diameter smaller than this critical diameter are *stable*. The stresses on a droplet are determined mostly by the relative Weber number:

$$\mathrm{We}_d \equiv \frac{\rho_a \left|\vec{U}_a - \vec{U}_d\right|^2 d}{\sigma_w}. \tag{3.11}$$

For breakup the critical Weber number, for cases neglecting droplet viscosity, is usually $\mathrm{We}_c \equiv 12$ ([Honsek et al., 2008, Pilch and Erdman, 1987].

Most models identify multiple types of breakup. For example, Pilch and Erdman [1987] identify five types, or modes, of breakup:

- vibrational breakup,
- bag breakup,
- bag-and-stamen breakup,
- sheet stripping, and
- wave crest stripping (followed by catastrophic breakup).

These five breakup modes are illustrated in Fig. 3.2 and a model based on the experiments is described in the next section.

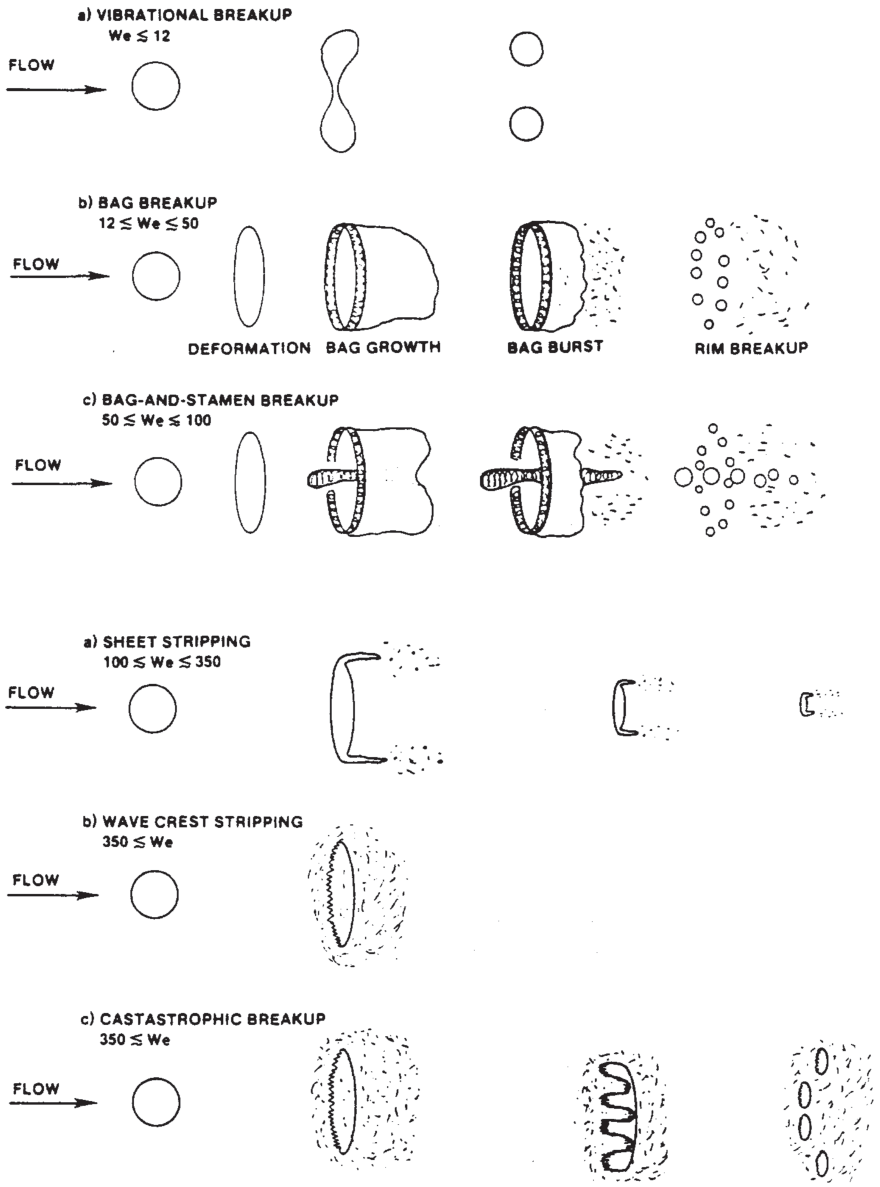

Figure 3.2: *Sketch of the various breakup modes [Pilch and Erdman, 1987]*

PILCH AND ERDMAN

One method for predicting droplet breakup is by Pilch and Erdman [1987]. It uses the critical Weber number, the stable diameter, and the critical resident time to determine breakup. A separate resident time is used for each of the five breakup modes. To this end a dimensionless time is defined as

$$T = t\frac{\left|\vec{U}_a - \vec{U}_d\right|\sqrt{\frac{\rho_a}{\rho_w}}}{d}. \tag{3.12}$$

The stable diameter can be estimated using

$$d_{stab} = \mathrm{We}_c\frac{\sigma_a}{\rho_a\left|\vec{U}_a - \vec{U}_d\right|^2}, \tag{3.13}$$

breakup will continue as long as the secondary droplets are still larger than the stable diameter. The resident times for the five breakup modes to reach total breakup, where $d \leq d_{stab}$, are then:

$$T = \begin{cases} 6\left(\mathrm{We}_d - 12\right)^{-0.25}: & 12 \leq \mathrm{We}_d \leq 18 \\ 2.45\left(\mathrm{We}_d - 12\right)^{-0.25}: & 18 \leq \mathrm{We}_d \leq 45 \\ 14.1\left(\mathrm{We}_d - 12\right)^{-0.25}: & 45 \leq \mathrm{We}_d \leq 351 \\ 0.766\left(\mathrm{We}_d - 12\right)^{-0.25}: & 351 \leq \mathrm{We}_d \leq 2670 \\ 5.5: & \mathrm{We}_d \geq 2670 \end{cases}. \tag{3.14}$$

TAB-METHOD

The Taylor analogy breakup (TAB) model from O'Rourke and Amsden [1987] is a widely used breakup model. In this model, breakup is assumed to occur due to internal vibration of a droplet. This vibration can lead to instability and breakup of the droplet.

The equation governing the (damped) vibration of a droplet is

$$F - kx - d\frac{\mathrm{d}x}{\mathrm{d}t} = m\frac{\mathrm{d}^2x}{\mathrm{d}t^2}. \tag{3.15}$$

In this equation d signifies the damping coefficient, not the diameter and x is the relative displacement of the equator of the droplet. Taylor's analogy

gives the coefficients:

$$\frac{F}{m} = C_F \frac{\rho_a \left|\vec{U}_a - \vec{U}_d\right|^2}{\rho_w r}, \tag{3.16a}$$

$$\frac{k}{m} = C_k \frac{\sigma_w}{\rho_w r^3}, \tag{3.16b}$$

$$\frac{d}{m} = C_d \frac{\mu_w}{\rho_w r^2}; \tag{3.16c}$$

with r the droplet radius; and C_F, C_k, and C_d chosen to match experimental data.

Droplet breakup, according to this model, occurs when the distortion of a droplet is greater than the critical ratio C_b of the droplet radius:

$$x > C_b r.$$

The most common assumption for the critical ratio is $C_b \equiv 0.5$. This means that breakup occurs when a droplet vibrates with a magnitude such that the north and south poles meet at the middle of a droplet.

Non-dimensionalizing using $y = \frac{x}{C_b r}$, and substituting Eq 3.16 into Eq. 3.15 gives:

$$\frac{\mathrm{d}^2 y}{\mathrm{d}t^2} = \frac{C_F}{C_b}\frac{\rho_a}{\rho_w}\frac{\left|\vec{U}_a - \vec{U}_d\right|^2}{r^2} - \frac{C_k \sigma_w}{\rho_w r^3} y - \frac{C_d \mu_w}{\rho_w r^2}\frac{\mathrm{d}y}{\mathrm{d}t}, \tag{3.17}$$

where breakup will now occur for a non-dimensional droplet deformation $y > 1$. Solving Eq. 3.17 for y is possible, assuming that the relative velocity is constant:

$$y(t) = \mathrm{We}_m + \mathrm{e}^{-t/t_d}\left[(y_0 - \mathrm{We}_m)\cos(\omega t) + \frac{1}{\omega}\left(\frac{\mathrm{d}y_0}{\mathrm{d}t} + \frac{y_0 + \mathrm{We}_m}{t_d}\right)\sin(\omega t)\right], \tag{3.18}$$

where the modified Weber number is

$$\mathrm{We}_m \equiv \frac{C_F}{C - kC_d}\mathrm{We}_d,$$

the damping frequency is

$$\frac{1}{t_d} = \frac{C_d}{2}\frac{\mu_w}{\rho_w r^2},$$

and the oscillation frequency is defined from

$$\omega^2 = C_k \frac{\sigma_w}{\rho_w r^3} - \frac{1}{t_d^2}.$$

The diameter of the secondary droplets after breakup is determined from energy conservation. Using the vibrational energy of the droplet, the Sauter mean radius of the secondary droplets is found to be

$$r_{32} = \frac{r}{1 + \frac{9Ky^2}{20} + \frac{\rho_w r^2 \left(\mathrm{d}y/\mathrm{d}t\right)^2}{\sigma}\frac{6K-5}{120}}; \tag{3.19}$$

with K the ratio of total energy in distortion and oscillation in the fundamental mode, of the order $K \approx 0.33$.

SPLASHING 3.2.3

The most important effect specific for SLD's is the splashing effect. Splashing is usually parameterized by the Weber number (Eq. 3.11) and the Reynolds number, or by a combination of Weber and Reynolds: the Ohnesorge number, which is similar to the Laplace number La. The Ohnesorge number is defined as:

$$\mathrm{Oh}_d \equiv \frac{1}{\sqrt{\mathrm{La}}} \equiv \frac{\sqrt{\mathrm{We}}}{\mathrm{Re}} \equiv \frac{\mu_a}{\sqrt{\rho_a \sigma_w d}}. \tag{3.20}$$

Splashing is usually characterized by a combination of Weber and Ohnesorge. Two widely used combinations can be found in literature:

Cossali The Cossali splashing parameter is defined as [Cossali et al., 1997]:

$$K = \mathrm{Oh}^{2/5}\mathrm{We}_n. \tag{3.21}$$

Yarin and Weiss The Yarin and Weiss splashing parameter is similar to the Cossali parameter [Yarin and Weiss, 1995]:

$$\begin{aligned} K_y &= \Lambda^{-3/8} \left(\mathrm{Oh}^{2/5}\mathrm{We}_n\right)^{5/16} \\ &= \left[\frac{3}{2}\left(\frac{\mathrm{LWC}}{\rho_w}\right)^{1/3}\right]^{-3/8} \left(\mathrm{Oh}^{2/5}\mathrm{We}_n\right)^{5/16}, \end{aligned} \tag{3.22}$$

where Λ is the droplet frequency, which functions as a measure for film thickness.

In both these combinations, a larger diameter d, as seen with SLD, increases the parameter; leading to a higher probability of a splashing event.

Both Cossali and Yarin and Weiss determined a critical value of their splashing parameter, any value above this critical level leads to a splashing event. The critical Cossali parameter is determined as a function of film thickness, which is mostly unknown in a numerical simulation. Yarin and Weiss found the critical value to be a constant:

$$K_{y,crit} = 17. \tag{3.23}$$

TRUJILLO

Besides the critical values for splashing, a complete model for the numerical simulation of splashing events needs more information: the number, size, direction, and velocity of the secondary droplets. These parameters are shown in Fig. 3.3. One of the first papers that attempts to model these parameters is by Trujillo et al. [2000]. His model was intended for fuel injection sprays. Trujillo et al. statistically analyzed several impingement experiments.

The splashing parameter used by Trujillo is taken from the work of Cossali, Eq. 3.21. An empirical relation for the critical value of this splashing parameter was determined by fitting data from Stow and Hadfield [1981] and Mundo et al. [1995]. When the splashing parameter K exceeds this critical value, the impinging droplet will splash. This relation is only valid for dry surface conditions and is a function of the non-dimensional surface roughness R_{nd}:

$$K_{c,dry} = 180 R_{nd}^{-0.35}, \tag{3.24}$$

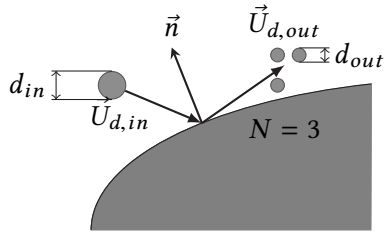

Figure 3.3: *Parameters involved in a splashing event*

where

$$R_{nd} \equiv \frac{R_a}{d_{in}}, \tag{3.25}$$

with R_a the average surface roughness.

To account for the wetting of the surface from previous droplet impacts, the data from Yarin and Weiss is used to estimate $K_{c,spray}$:

$$\frac{K_{c,spray}}{K_{c,dry}} = \kappa \approx 3.0, \tag{3.26}$$

assuming that the ratio κ remains constant for varying surface roughnesses R_{nd}.

Stow and Stainer [1977] reported a linear correlation between kinetic energy and the number of secondary droplets. This linear relation is extended by fitting Trujillo's experimental data, obtaining a relation between the Cossali splashing parameter K and the number of secondary droplets. Any influence from surface roughness is present in the parameter $K_{c,dry}$:

$$N = \frac{1}{22}\left[0.0437\left(K\left(\frac{\left|\vec{U}_{d,in}\right|}{\vec{U}_{d,in}\cdot\vec{n}}\right)^2 - K_{c,dry}\right) - 44.92\right]. \tag{3.27}$$

The number of secondary droplets also depends on the incident angle of the incoming droplet:

$$\theta = \arcsin\left(\frac{\vec{U}_{d,in}\cdot\vec{n}}{\left|\vec{U}_{d,in}\right|}\right). \tag{3.28}$$

Note that the relation of the number of secondary droplets is linear with respect to the splashing parameter, if the incident angle is kept constant.

By applying a Gaussian distribution to the data from Mundo et al., a relation for the mean tangential velocity and mean normal velocity can be found:

$$\frac{\vec{U}_{d,out} \cdot \vec{t}}{\vec{U}_{d,in} \cdot \vec{t}} = 0.85 + 0.0025\,\theta, \tag{3.29a}$$

$$\frac{\vec{U}_{d,out} \cdot \vec{n}}{\vec{U}_{d,in} \cdot \vec{n}} = 0.12 + 0.002\,\theta; \tag{3.29b}$$

where a restriction to the incident angle θ of a droplet, is inherited from Mundo et al.: $4° < \theta < 65°$.

From the work of Yarin and Weiss, a relation for the amount of splashed mass is determined, expressed as the mass loss coefficient ϕ. For convenience the splashing parameters from Yarin and Weiss are converted to Cossali's splashing parameter:

$$\begin{aligned}\phi = \frac{m_{out}}{m_{in}} &= 0.8\left\{1 - \exp\left[-0.85\left(K_y - K_{y,crit}\right)\right]\right\} \\ &= 0.8\left\{1 - \exp\left[-0.85\left(\Lambda^{-3/8}K^{5/16} - \Lambda^{-3/8}K_{c,spray}^{5/16}\right)\right]\right\}.\end{aligned} \tag{3.30}$$

This equation is graphically presented in Fig. 3.4.

From mass conservation the average diameter of the secondary droplets d_{out} can be determined using N, ϕ, and d_{in}:

$$\phi\rho_w\frac{\pi d_{in}^3}{6} = N\rho_w\frac{\pi d_{out}^3}{6}, \tag{3.31}$$

so that

$$d_{out} = \left(\frac{\phi}{N}\right)^{1/3} d_{in}. \tag{3.32}$$

The mass loss coefficient can be used to correct the local catching efficiency for the amount of water that moves away from the surface due to splashing. The average diameter and velocity of the secondary droplets can be used to calculate the trajectory of the secondary droplets. Note that for the Trujillo model, the mass loss increases very rapidly to an asymptote of 0.8.

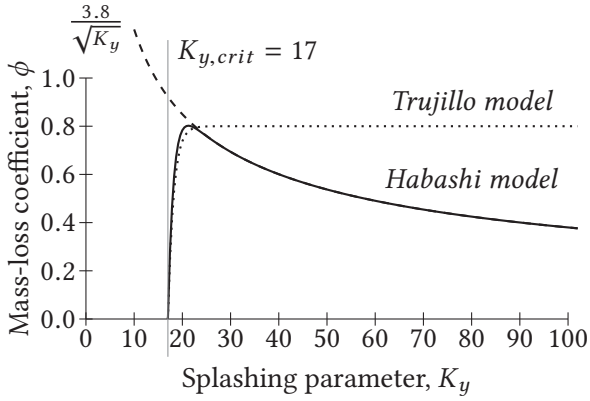

Figure 3.4: *Mass loss coefficient as a function of splashing parameter*

HABASHI

Honsek et al. [2008]—commonly known as the Habashi model—addressed the over-prediction of mass loss by calibrating Trujillo's mass loss function to SLD conditions, resulting in an equation very similar to Eq. 3.30, replacing the constant 0.8 by $\frac{3.8}{\sqrt{K_y}}$:

$$\begin{aligned}\phi &= \left(\frac{3.8}{\sqrt{K_y}}\right)\left\{1-\exp\left[-0.85\left(K_y - K_{y,crit}\right)\right]\right\} \\ &= 3.8\Lambda^{3/16}K^{-5/32}\left\{1-\exp\left[-0.85\Lambda^{-3/8}\left(K^{5/16}-K_c^{5/16}\right)\right]\right\}.\end{aligned} \tag{3.33}$$

The $\sqrt{K_y}$ term in this equation ensures that for increasing splashing parameter K_y the mass loss coefficient decreases from the 0.8 asymptote. A graphical representation of this function is given in Fig. 3.4. Note that for $K_y > 23$ the mass loss equation can be approximated (within 1%) by:

$$\phi \approx \frac{3.8}{\sqrt{K_y}} = 3.8\Lambda^{3/16}K^{-5/32}: \quad K_y > 23. \tag{3.34}$$

3.2.4 REBOUND

Rebound is an SLD effect that is strongly related to splashing. In stead of the splashing event resulting in multiple smaller droplets a rebound results in a

single secondary droplet moving away from the surface, without depositing mass. Rebounding takes place mostly near the impingement limits and has the effect of moving the impingement limits further upstream, reducing the impingement area.

BAI AND GOSMAN

The rebound model is taken from the implementation of Honsek et al. [2008], using the model by Bai and Gosman [1995]. A splashing threshold is defined using the droplet Weber number. From experiments, a minimum and maximum value has been found, where the maximum value depends on the Laplace—or Ohnesorge—number:

$$10 \leq \mathrm{We}_d \leq 1320\,\mathrm{La}^{-0.18} = 1320\,\mathrm{Oh}_d^{0.36}. \tag{3.35}$$

Bai and Gosman also determined relations for the secondary velocity, these relations are similar to relations for the velocities of a splashing droplet described in Eq. 3.29. Note that the tangential velocity does not depend on the angle of incidence:

$$\frac{\vec{U}_{d,out} \cdot \vec{t}}{\vec{U}_{d,in} \cdot \vec{t}} = \frac{5}{7}, \tag{3.36a}$$

$$\frac{\vec{U}_{d,out} \cdot \vec{n}}{\vec{U}_{d,in} \cdot \vec{n}} = -\left(0.9930 - 0.0307\,\theta' + 0.0272\,\theta'^2 - 0.0086\,\theta'^3\right), \tag{3.36b}$$

where $\theta' = 90 - \theta$.

For a rebound event, the diameter remains unchanged: a single droplet rebounds from the surface, leading to all mass being lost:

$$d_{out} = d_{in}, \quad \phi = 1. \tag{3.37}$$

EULERIAN DROPLET METHOD

4

This chapter eludes on the implementation of the SLD models described in the previous chapters. Specifically, it explains the development of a new ice accretion calculation method, using an Eulerian frame. This in contrast with the Lagrangian frame of 2DFOIL-ICE. The Eulerian method has been named *Droplerian*, an aggregation of **drop**lets and Eu**lerian**.

EULERIAN DROPLET TRACKING 4.1

The 2DFOIL-ICE method is based on Lagrangian droplet tracking, in which the (potential) flow field is calculated using a panel-method. This has some limitations, especially for cases in which multiple-element airfoil geometries are represented. Due to the potential-flow model in 2DFOIL-ICE, the geometry of multiple-element airfoils often has to be approximated in order to cope with the viscosity dominated flow solutions in cove regions. This can be achieved by allowing only a single sharp edge on each element, and by determining cove bounding streamlines as integral parts of the closed element geometries.

A second problem can be the process of finding droplet trajectories that impinge on one of the airfoil elements. This can become a time consuming task.

To reduce both of these limitations an Eulerian droplet tracking method has been developed. The Eulerian method accepts flow field data from any available flow model, e.g., potential-flow such as used in 2DFOIL-ICE, but also flow field solutions based on the Euler equations or the full Navier-Stokes equations. The flow field is used as input to calculate a droplet velocity and droplet density field on a grid around the airfoil. For the Eulerian method, discrete droplet trajectories do not need to be calculated, reducing the computational load, while allowing a detailed investigation of the droplet variables close to the airfoil.

A further reason for developing the Eulerian method is the relatively easy extension towards three-dimensional geometries compared to Lagrangian methods.

The output needed from the droplet tracking method should be suited as input for the icing method. For the icing method only two quantities related to the impinging droplets are needed: the rate of mass of water impinging locally on the airfoil surface, and the rate of kinetic energy that is associated with the impinging droplets. The local rate of impinging mass can be obtained from the local catching efficiency β. From the velocity of the impinging droplets the rate of kinetic energy due to the impinging droplets can be calculated.

For Lagrangian methods the local catching efficiency is defined as the ratio of the rate of impinging mass divided by the rate of impinging mass had the droplet trajectories been straight lines, as was shown in Eq. 2.7

$$\beta = \frac{\mathrm{d}y}{\mathrm{d}s},$$

and in Fig. 2.1, assuming that the mass of the droplets between two droplet trajectories remains constant; given a fixed value of $\mathrm{d}y$, the smaller the contour element $\mathrm{d}s$ the larger the rate of impinging mass and therefore, β.

For an Eulerian method, since we do not (necessarily) compute individual droplet trajectories, this approach cannot be applied. Using the liquid water content (LWC) of the cloud, the following relation depending only on the local droplet density ρ_d and local droplet velocity $\vec{U}_d$ can be derived:

$$\beta = \frac{\rho_d \vec{U}_d \cdot \vec{n}}{\mathrm{LWC} \left| \vec{U}_{d,\infty} \right|}, \tag{4.1}$$

where the local droplet density ρ_d is the volume fraction of water contained in the droplets α multiplied with the local water density ρ_w, at the airfoil of wing surface:

$$\rho_d = \alpha \rho_w. \tag{4.2}$$

Equation 4.1 contains the rate of impinging mass of liquid water per square meter $\rho_d \vec{U}_d \cdot \vec{n}$ (see Fig. 4.1), which can be used directly as input for the icing model.

To calculate both ρ_d and $\vec{U}_d$, the droplets are considered as a second fluid phase. Solving the mass and momentum balances for a discretized

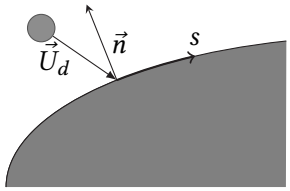

Figure 4.1: *Droplet velocity $\vec{U}_d$ and surface normal $\vec{n}$*

domain provides these local quantities. One of the source terms for the momentum balance will be the drag force, since this is the main driving force for the droplet phase. The equations for conservation of mass and conservation of momentum for the droplet phase are:

$$\frac{\partial \rho_d}{\partial t} + \vec{\nabla} \cdot \rho_d \vec{U}_d = 0, \tag{4.3}$$

$$\frac{\partial \rho_d \vec{U}_d}{\partial t} + \vec{\nabla} \cdot \left(\rho_d \vec{U}_d\right) \vec{U}_d = \rho_d \vec{f}_D + \rho_d \left(1 - \frac{\rho_a}{\rho_w}\right) \vec{g}; \tag{4.4}$$

where the only other source-term considered, besides the drag force $\vec{f}_D$, is due to gravity and buoyancy. For the present case other forces, such as lift force and Basset history force, are neglected.

The drag force is expressed in terms of the drag coefficient C_D:

$$\vec{f}_D = \frac{\rho_a \left|\vec{U}_a - \vec{U}_d\right| \left(\vec{U}_a - \vec{U}_d\right) A_d C_D}{2 \rho_w V_d}, \tag{4.5}$$

where C_D is usually a function of droplet diameter and the Reynolds number based on the relative droplet velocity Re_d (Eq. 2.3). The drag force D is taken from Eq. 2.2. The expression for the drag coefficient can range from an expression for small diameter droplets to special relations for deforming droplets (SLD diameter droplets). In the current method C_D is initially identical to the drag coefficient from the Lagrangian method. Equation 2.4 is repeated here for clarity [Langmuir and Blodgett, 1946]:

$$\frac{C_D \mathrm{Re}_d}{24} = 1 + 0.0197 \mathrm{Re}_d^{0.63} + 2.6 \cdot 10^{-4} \mathrm{Re}_d^{1.38},$$

which is valid for $\mathrm{Re}_d < 1000$.

The equations for the Eulerian method are solved numerically by employing a finite-volume method based on similar numerical flow simulation methods [Kelleners, 2007, Koop, 2008]. This edge-based finite-volume method uses an unstructured grid and is suited for both two-dimensional and three-dimensional domains, discretized using a combination of element types. The flow field of the air surrounding the airfoil or wing is used only as input, since it is assumed one-way coupling between the air and droplet phase is adequate for the present purpose. The flow solution can be obtained from any available flow solver.

4.2 IMPLEMENTATION

The base of the Eulerian droplet tracking method is a 2D Lagrangian droplet tracking method. The first implementation has been based on this 2D method, but implemented in a 3D frame.

4.2.1 TIME STEP

For a Navier-Stokes, edge-based, finite-volume method; for *non-local* or *global* time stepping the maximum time step is defined as follows:

$$\max \Delta t \equiv \frac{\min \Delta x}{\left|\vec{U}\right| + a}, \tag{4.6a}$$

where Δx is a characteristic length scale of a control volume, such as the distance or radius through a grid cell. The maximum time step can be described as: the time needed for "information" to travel through the smallest cell possible, at the fastest speed possible. For *local* time stepping the time step can be formulated as:

$$(\max \Delta t)_i \equiv \frac{(\min \Delta x)_i}{\left|\vec{U}_i\right| + a_i}, \tag{4.6b}$$

where i denotes the quantities belonging to the i^{th} grid-cell.

For the Eulerian droplet tracking method this methodology cannot be employed. The considered field actually consists of a disperse medium. The speed of sound has nothing to do with the speed at which information

travels from one droplet to another; or from one grid-cell or control volume containing droplets, to the next.

Analyzing the system of equations posed by Eq. 4.3 and Eq. 4.4, the maximum time step is related to the eigenvalues of this system. This would mean that for this system of equations the information velocity would be $\vec{U}_d$. For the Navier-Stokes equations, the speed of sound is introduced via the pressure-gradient term, which is not present in the system of equations for the droplets. This gives the following relations for the maximum global time step and the maximum local time step, respectively:

$$\max \Delta t \equiv \frac{\min \Delta x}{\left|\vec{U}_d\right|}, \tag{4.7a}$$

$$\left(\max \Delta t\right)_i \equiv \frac{\left(\min \Delta x\right)_i}{\left|\vec{U}_{d,i}\right|}. \tag{4.7b}$$

MULTI-DISPERSE DROPLET DISTRIBUTIONS 4.2.2

In the original Lagrangian method, a mono-disperse droplet distribution was employed. This meant that the entire droplet cloud was simulated using droplets with a single diameter, usually with a diameter equal to the MVD. For clouds with smaller droplets this is an acceptable assumption, the droplet distribution is very dense around the MVD. Furthermore, it is assumed that droplets do not change their size during the droplet tracking phase. However, for larger droplets, especially for SLD, the size of the droplets *can* change during the droplet tracking phase, e.g., after a splashing or a breakup event. Furthermore, typical clouds containing SLD often have a bimodal droplet size spectrum. To cope with these phenomena the resulting Eulerian droplet tracking equations (Eq. 4.3, 4.4) are solved for a multi-disperse droplet distribution, separated in multiple droplet-bins. For each droplet-bin in the distribution, a separate set of equations is solved; each bin corresponding to a single specific droplet diameter.

The results of ρ_d and $\vec{U}_d$ for each droplet-bin are combined in a single distribution for the catching efficiency β, which is subsequently used in the icing method, using the fraction of the total LWC, F_i for the specific

droplet-bin. The sum of F_i for all droplet-bins has to be equal to one:

$$\sum_{i=1}^{N_{bin}} F_i = 1, \tag{4.8}$$

with N_{bin} the number of droplet-bins. Then the catching efficiency becomes

$$\beta = \sum_{i=1}^{N_{bin}} F_i \beta_i. \tag{4.9}$$

In order to accommodate the splashing and re-injection of droplets, it is necessary to compute the droplet bins in a sequential, largest first, order. This ensures that secondary droplets resulting from splashing events in bin i, possibly forming multiple *smaller* secondary droplets, can be re-injected into bin $i + 1$. The results from each bin are stored separately because the velocity and droplet density of each bin are needed to calculate the impinging kinetic energy for the ice accretion method.

4.2.3 SPLASHING METHOD

To implement the additional splashing method, a new subroutine has been added to the computational method. A graphical description of the splashing and rebound method can be found in Fig. 4.2. Based on the local droplet density ρ_d and the local droplet velocity $\vec{U}_d$, the subroutine determines the mass loss coefficient ϕ and the secondary velocity $\vec{U}_{d,out}$. Since the splashing models from Trujillo (section 3.2.3) and Habashi (section 3.2.3) consider splashing as an event in two dimensions (normal and tangential), information about orientation of the impingement surface is also needed. The models also provide the number of secondary droplets, leading to a secondary diameter d_{out}. These inputs and outputs are summarized in Table 4.1.

The first step is to decompose the droplet velocity $\vec{U}_d$ at the impact point in a normal and tangential component, as shown in Fig. 4.3. The process to find the normal component is straightforward, using the surface normal vector $\vec{n}$:

$$U_{n,in} = \vec{U}_{d,in} \cdot \vec{n}. \tag{4.10}$$

The tangential component of the droplet velocity depends on the angle of the trajectory of the incoming droplet with the surface. The normal

Table 4.1: *Splashing method input and output*

input	output
ρ_d	ϕ
$\vec{U}_{d,in}$	$\vec{U}_{d,out}$
d_{in}	d_{out}
$\vec{n}$	

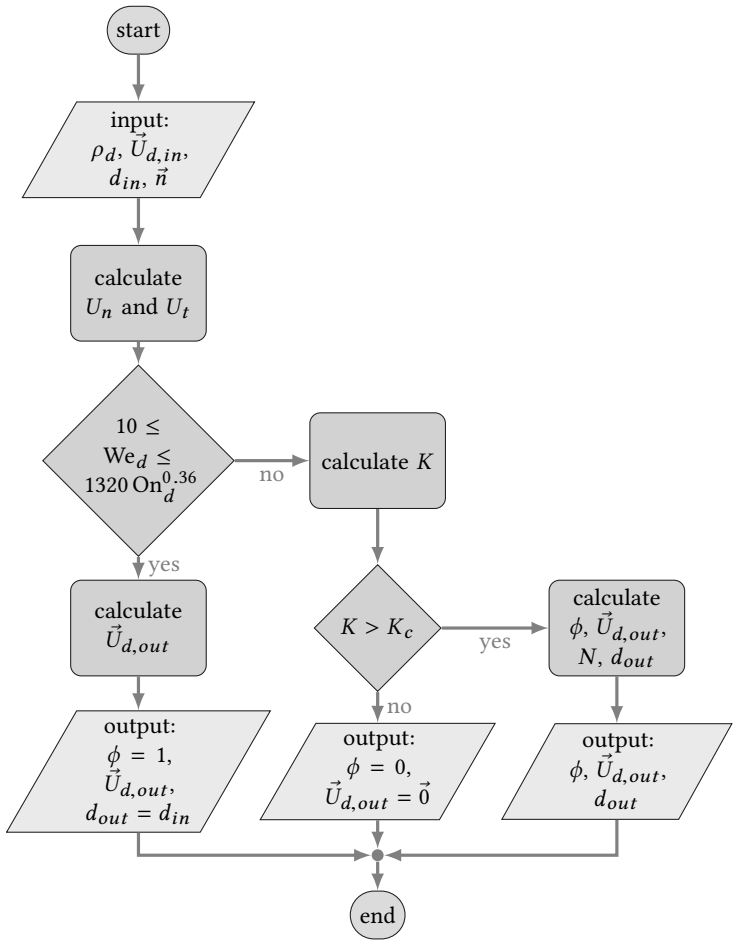

Figure 4.2: *Flow chart of the subroutine for calculating the splashing and rebound occurring for a single droplet-bin at a control volume on the surface of the airfoil or wing*

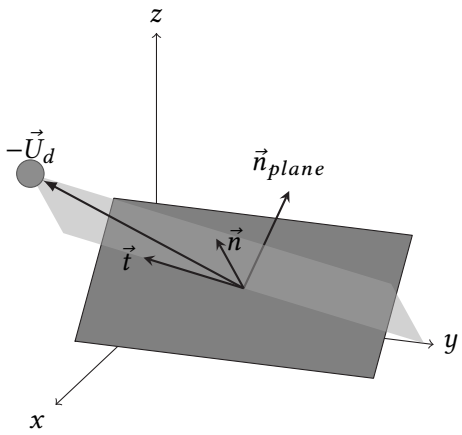

Figure 4.3: *Plane spanned by the velocity of an incoming droplet $\vec{U}_{d,in}$ and the surface normal $\vec{n}$ at the impact point on the surface*

vector of a plane spanned by the incoming droplet velocity $\vec{U}_{d,in}$ and the surface normal vector $\vec{n}$ follows from

$$\vec{n}_{plane} = \frac{\vec{n} \times \vec{U}_{d,in}}{\left|\vec{n} \times \vec{U}_{d,in}\right|}. \tag{4.11}$$

The tangential vector needed for the splashing model is the vector perpendicular to this normal vector $\vec{n}_{plane}$ and the surface normal vector $\vec{n}$:

$$\vec{t}_{plane} = \frac{\vec{n} \times \vec{n}_{plane}}{\left|\vec{n} \times \vec{n}_{plane}\right|}. \tag{4.12}$$

The tangential component of the velocity is then:

$$U_{t,in} = \vec{U}_{d,in} \cdot \vec{t}_{plane}. \tag{4.13}$$

The normal component of the velocity is used in the splashing criterion from Eq. 3.26, using Eq. 3.24 and Eq. 3.21. Splashing occurs if

$$K > K_{c,spray}. \tag{4.14}$$

If no splashing occurs: $\phi = 0$ and the subroutine ends. However, if splashing does occur, ϕ is determined using Eq. 3.33, followed by a calculation

of the average velocity of the secondary droplets using Eq. 3.29. The secondary droplet velocity is then assembled from the normal and tangential components:

$$\vec{U}_{d,out} = U_{d,out} \cdot \vec{n} + U_{d,out} \cdot \vec{t}_{plane}. \tag{4.15}$$

Finally, the number of secondary droplets N is determined using Eq. 3.27. If $N > 1$ the secondary diameter d_{out} is determined using Eq. 3.32. If $N \leq 1$, $d_{out} = d_{in}$.

REBOUND MODEL 4.2.4

The rebound model is implemented as a special case of splashing, as shown in Fig. 4.2. Apart from the splashing threshold, in the same splashing subroutine, a check is performed (Eq. 3.35) to determine if a rebound event will take place. If a rebound event is detected $\phi = 1$, $N = 1$ and $d_{out} = d_{in}$. The components of the secondary velocities for the rebounded droplets are determined using Eq. 3.36.

RE-INJECTION OF SPLASHED DROPLETS 4.2.5

Droplets that splash—or rebound, for re-injection this is equivalent—should in most cases be re-injected into the droplet flow domain. It could be that these secondary droplets impinge on the surface at another location in a later stage of the impingement process. The re-injection of droplets depends on the diameter of the secondary droplets that are formed during a splashing or rebound event.

In case of a rebound event, for which $d_{out} = d_{in}$, the droplet is re-injected into the same bin as it originated from. For splashing events, however, secondary droplets will always be smaller than the originating droplets: $d_{out} < d_{in}$. The secondary droplets are re-injected into a bin representing a smaller diameter. The actual re-injection bin is chosen to be the bin representing the diameter closest to that of the secondary droplet diameter:

$$bin_{out} = \begin{cases} bin_{in} : & \text{rebound} \\ bin_{in} + \text{minloc}[d_{out} - d_{bin,i}] : & \text{splash} \end{cases}, \tag{4.16}$$

where $i = bin_{in} + 1, bin_{in} + 2, \ldots, N_{bin}$. Also, $d_{bin,i}$ is the diameter represented by bin i; bin_{in} is the bin the primary droplet originated from; and

`minloc` is the FORTRAN-like function, returning the relative position of the entry in the array with the minimum value of the argument of the function.

The extraction and injection of mass and momentum is managed by keeping separate arrays of data; [mlc], which stands for mass loss coefficient and [mri], which stands for mass re-injected:

$$\mathsf{mlc} = \phi_{i,j} \qquad [N_{bin} \times N_{cell}]\,, \tag{4.17}$$

$$\mathsf{mri} = \mathsf{mri}_{i,k,j} + \phi_{i,j}\rho_{d,i,j} \qquad [N_{bin} \times N_{bin} \times N_{cell}]\,. \tag{4.18}$$

where $\phi_{i,j}$ is ϕ from bin i, cell j; and $\rho_{d,i,j}$ is ρ_d from bin i, cell j, into bin k (based on the closest diameter from Eq. 4.16).

These arrays are filled during the numerical simulation process, at the beginning of a simulation, the mass lost and re-injected into each cell equals zero. At each moment in time, the amount of mass injected into bin k cell j becomes:

$$mri_{k,j} = \sum_{i=1}^{N_{bin}} \mathsf{mri}_{i,k,j}. \tag{4.19}$$

Similar to the array of re-injected mass [mri], there are also three arrays containing the re-injected momentum:

$$\left.\begin{aligned} \mathsf{uri} &= \mathsf{uri}_{i,k,j} + \phi_{i,j}\rho_{d\,i,j}u_{d\,i,j} \\ \mathsf{vri} &= \mathsf{vri}_{i,k,j} + \phi_{i,j}\rho_{d\,i,j}v_{d\,i,j} \\ \mathsf{wri} &= \mathsf{wri}_{i,k,j} + \phi_{i,j}\rho_{d\,i,j}w_{d\,i,j} \end{aligned}\right\} [N_{bin} \times N_{bin} \times N_{cell}]\,, \tag{4.20}$$

with bin-totals:

$$uri_{k,j} = \sum_{i=1}^{N_{bin}} \mathsf{uri}_{i,k,j} \quad vri_{k,j} = \sum_{i=1}^{N_{bin}} \mathsf{vri}_{i,k,j} \quad wri_{k,j} = \sum_{i=1}^{N_{bin}} \mathsf{wri}_{i,k,j}. \tag{4.21}$$

Example.
Both arrays are initialized:

$$\mathsf{mlc} = \mathsf{mri} = 0.$$

If droplets from bin 1, cell 1 will splash as secondary droplets into bin 3 (based on Eq. 4.16), they will populate both matrices as follows, using

Eq. 4.17 and Eq. 4.18:

$$\begin{aligned} \mathrm{mlc}_{1,1} &= 0.8, \\ \mathrm{mri}_{1,3,1} &= 0 + 0.8\,\rho_{d,1,1}. \end{aligned}$$

Suppose droplets from bin 2 also splash into bin 3:

$$\begin{aligned} \mathrm{mlc}_{2,1} &= 0.6, \\ \mathrm{mri}_{2,3,1} &= 0.8\,\rho_{d,1,1} + 0.6\,\rho_{d,2,1}. \end{aligned}$$

The amount of mass injected into bin 3, cell 7 becomes (Eq. 4.19):

$$mri_{3,7} = \sum_{i=1}^{N_{bin}} \mathrm{mri}_{i,3,7}.$$

BOUNDARY CONDITIONS 4.2.6

With respect to the boundary conditions, the boundary condition at the surface of the airfoil or wing requires special attention. In order to calculate a catching efficiency the normal component of the droplet velocity at the airfoil surface is needed. However, when the normal component of the droplet velocity is negative (using the definition from Fig. 4.1), i.e., away from the airfoil, droplets should not be created from the surface of the airfoil. This leads to a boundary condition on the surface of the airfoil, which depends on the sign of the normal component of the droplet velocity.

For a normal component of the droplet velocity directed away from the airfoil the following boundary conditions are applied:

$$\vec{U}_d \cdot \vec{n} \geq 0 : \quad \psi_{wall} = 0, \tag{4.22a}$$

where ψ is the variable of the considered governing equation; either ρ_d or $\rho_d \vec{U}_d$. In case the normal component of the droplet velocity at the surface is directed into the airfoil the values at the wall ψ_{wall} are calculated by extrapolation from the values at the center of the finite-volume next to the airfoil surface ψ_0:

$$\vec{U}_d \cdot \vec{n} < 0 : \quad \psi_{wall} = \psi_0 + (\vec{x}_{wall} - \vec{x}_0) \cdot \vec{\nabla}\psi_0. \tag{4.22b}$$

For the re-injection of droplets the values at the wall have to be increased to contain the added amount of mass or momentum:

$$\sum_{i=1}^{N_{bin}} \mathrm{mri}_{i,k,j} > 0 : \quad \psi_{wall,j} = \psi_{wall,j} + \begin{cases} \sum_{i=1}^{N_{bin}} \mathrm{mri}_{i,k,j} : & \rho_d \\ \sum_{i=1}^{N_{bin}} \mathrm{uri}_{i,k,j} : & \rho_d u \\ \sum_{i=1}^{N_{bin}} \mathrm{vri}_{i,k,j} : & \rho_d v \\ \sum_{i=1}^{N_{bin}} \mathrm{wri}_{i,k,j} : & \rho_d w \end{cases}, \tag{4.23}$$

with k the considered bin and j the considered cell next to the surface.

5 ICE ACCRETION METHOD IN THREE DIMENSIONS

One of the major advantages of an Eulerian approach is the easy extension of the droplet tracking method to three-dimensions. However, this also requires a method for calculating the ice accretions in 3D.

5.1 BOUNDARY ORDERING

In 2D, the ice accretion method is fairly simple: starting at the stagnation point, the temperature T_s and freezing fraction f can be calculated, one control volume after another. This assumes that the air flowing along the surface forces the water film from the stagnation point in downstream direction. In 3D the stagnation point has become a stagnation line, leading to a 2D surface flow.

This means that the sequential ordering of control volumes becomes far less trivial. This would mean that the surface flow could; either be solved iteratively, or, an alternative ordering for the control volumes on the surface has to be found. In order to save on computational cost that would be implied by solving the surface flow iteratively, while recursively iterating on the temperature, the order of the boundary control volumes will be determined.

Considering the surface flow on an airfoil: similar to the 2D case, the surface flow starts at a stagnation panel, continuing downstream in multiple directions. Assuming again that the direction of the surface flow is completely determined by the flow of air along the surface:

$$\frac{\vec{U}_{s,i}}{\left|\vec{U}_{s,i}\right|} = \frac{\vec{U}_{a,i}}{\left|\vec{U}_{a,i}\right|}, \tag{5.1}$$

for the i^{th} control volume. Here $\vec{U}_s$ is the flow along the surface.

This means that by following the flow of air along the surface, the order in which the surface flow passes through the control volumes can be determined. As an intermediate step an array [rank] can be determined, starting at 1, increasing by 1 for each control volume the flow has passed.

As a first step, the approximate stagnation point (or stagnation line in 3D) is determined:

$$\mathrm{rank}_i = 1 : \quad \begin{cases} u_{a,i} < 1 \times 10^{-5} & \& \quad v_{a,i} < 1 \times 10^{-5} \\ u_{a,i} < 1 \times 10^{-5} & \& \quad w_{a,i} < 1 \times 10^{-5} \\ v_{a,i} < 1 \times 10^{-5} & \& \quad w_{a,i} < 1 \times 10^{-5} \end{cases} . \tag{5.2}$$

Starting from these points, which are most likely stagnation points, the flow can be followed along the surface in downstream direction, numbering the control volumes consecutively: if the velocity of the flow is in the same direction as the vector from one control volume to the next, the rank is determined. This process is repeated until no control volumes change rank. This is clarified in Algorithm 5.1 and illustrated in Fig 5.1.

Input: Initial ranking
Output: Final ranking
changed = **True**;
while *changed* **do**
    changed = **False**;
    for $i = 1, N_{conn}$ **do**
        $A =$ element left of i;
        $B =$ element right of i;
        if $\vec{U}_{a,A} \cdot (\vec{x}_B - \vec{x}_A)$ **and** $\mathrm{rank}_B < \mathrm{rank}_A + 1$ **then**
            $\mathrm{rank}_B = \mathrm{rank}_A + 1$;
            if not *changed* **then** *changed* = **True**;
            ;
        else if $\vec{U}_{a,B} \cdot (\vec{x}_A - \vec{x}_B)$ **and** $\mathrm{rank}_A < \mathrm{rank}_B + 1$ **then**
            $\mathrm{rank}_A = \mathrm{rank}_B + 1$;
            if not *changed* **then** *changed* = **True**;
            ;

Algorithm 5.1: Rank calculation

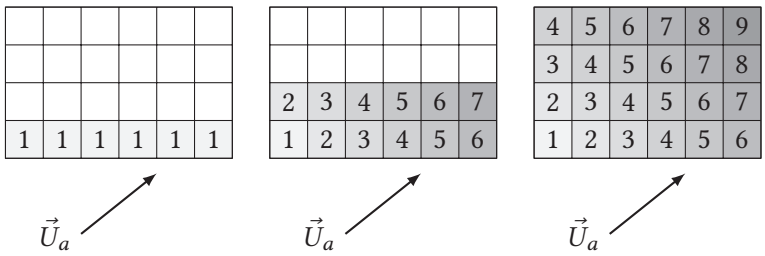

(a) *Initial values, stagnation line* ***(b)*** *First iteration* ***(c)*** *Last iteration*

Figure 5.1: *Illustration of rank calculation on a flat plate on a flat plate with uniform surface flow field*

The order of calculation is then determined by looping over all ranked cells, shown in Algorithm 5.2 and Fig. 5.2. The order-counter starts at $\text{order}_i = 1$, for the first cell i, with $\text{rank}_i = 1$. It increases for every cell with $\text{rank}_i = 1$. If all cells have been checked, the process is repeated for $\text{rank}_i = 2$. Note that the order can change depending on the order of the grid cells.

Input: Final ranking
Output: Order
$k = 1$;
while $k \leq \text{maxval}\,[\text{rank}]$ **do**
  $j = 1$;
  for $i = 1, N_{cell}$ **do**
    if $\text{rank}_i = k$ **then**
      $\text{order}_i = j$;
      $j = j + 1$;

Algorithm 5.2: Order calculation

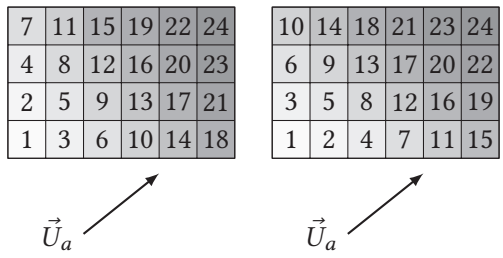

(a) *Cells ordered up-down-left-right*

(b) *Cells ordered left-right-up-down*

Figure 5.2: *Illustration of order calculation on a flat plate with uniform surface flow field*

The resulting array [order] contains the surface element numbers, ordered in flow direction, such that:

$$\begin{bmatrix} \text{order}_1 \\ \text{order}_2 \\ \vdots \\ \text{order}_{N_{cell}} \end{bmatrix} = \begin{bmatrix} \text{first cell to process} \\ \text{second cell to process} \\ \vdots \\ \text{last cell to process.} \end{bmatrix}$$

5.2 CATCHING EFFICIENCY CALCULATION

Apart from the preprocessing of the boundary control volumes, the catching efficiency has to be determined on the surface. For each control volume on the surface the catching efficiency is found using Eq. 4.1:

$$\begin{aligned} \beta &= \frac{\rho_d \vec{U}_d \cdot \vec{n}}{\text{LWC} \left| \vec{U}_{d,\infty} \right|} \\ \beta_i &= \frac{\rho_{d,i} \vec{U}_{d,i} \cdot \vec{n}_i}{\text{LWC} \left| \vec{U}_{d,\infty} \right|}. \end{aligned} \tag{5.3}$$

Any droplets that splash or rebound are already accounted for due to the change in mass and momentum introduced in Eq. 4.23, so the mass loss coefficient should not be included in Eq. 5.3.

MESSINGER METHOD 5.3

With the ordering of the boundary control volumes and the catching efficiencies known, it is possible to perform the calculation for the heat and mass balance in every control volume. Because this is a 3D method, the Messinger method has to be adapted.

MASS FLOW 5.3.1

The Messinger method assumes a 2D flow, with the surface flow entering the control volume (CV) from one side and leaving it at the other side as run-back water. This was demonstrated in Fig. 2.2. In 3D, the surface flow enters and leaves as determined by the surface flow direction. However, for the local mass and energy balances the control volume is still considered 2D, see Fig 5.3. The 3D flow comes into play in determining which control volumes receive the run back mass going out of the current control volume. The mass flowing out of the control volume, $\dot{m}_{out}$, has to be converted to a 3D vector:

$$\vec{\dot{m}}_{out,i} = \dot{m}_{out,i} \frac{\vec{U}_{a,i}}{\left|\vec{U}_{a,i}\right|}, \tag{5.4}$$

such that

$$\dot{m}_{in,B} = \sum_{i=1}^{N_{conn}} \dot{m}_{out,A} \frac{\vec{U}_{a,B}}{\left|\vec{U}_{a,B}\right|} \cdot \vec{n}_{A,B}, \tag{5.5}$$

where N_{conn} is the number of edges of the surface element connected to other elements, $\vec{U}_{a,B}$ is the air velocity of neighboring element B for edge i, and $\vec{n}_{A,B}$ is the normal on edge i.

Assuming that all surface flow is instantaneous, Algorithm 5.3 can be used to determine the inflow into every control volume.

Using this adapted mass flow method the Messinger method can be applied otherwise unaltered. This results in an ice thickness for each surface element. Projecting these ice thicknesses in the direction of the surface normal gives an ice accretion shape in three dimensions.

Input: Order, $\dot{m}_{out,i}$
Output: $[\dot{m}_{in}]$
$UX = 0$;
for $j = 1, N_{conn}$ **do**
    $A =$ element left of j;
    $B =$ element right of j;
    $UXj = \frac{1}{2}\left(\vec{U}_{a,A} + \vec{U}_{a,B}\right) \cdot \frac{\vec{x}_B - \vec{x}_A}{|\vec{x}_B - \vec{x}_A|}$;
    if $A == i$ **and** $UXj > 0$ **then**
        $UX = UX + UXj$;
    else if $B == i$ **and** $UXj < 0$ **then**
        $UX = UX - UXj$;
for $j = 1, N_{conn}$ **do**
    $A =$ element left of j;
    $B =$ element right of j;
    $UXj = \frac{1}{2}\left(\vec{U}_{a,A} + \vec{U}_{a,B}\right) \cdot \frac{\vec{x}_B - \vec{x}_A}{|\vec{x}_B - \vec{x}_A|}$;
    if $A == i$ **and** $UXj > 0$ **then**
        $\dot{m}_{in,B} = \dot{m}_{in,B} + \frac{UXj}{UX}\dot{m}_{out,A}$;
    else if $B == i$ **and** $UXj < 0$ **then**
        $\dot{m}_{in,A} = \dot{m}_{in,A} - \frac{UXj}{UX}\dot{m}_{out,B}$;

Algorithm 5.3: Inflow calculation

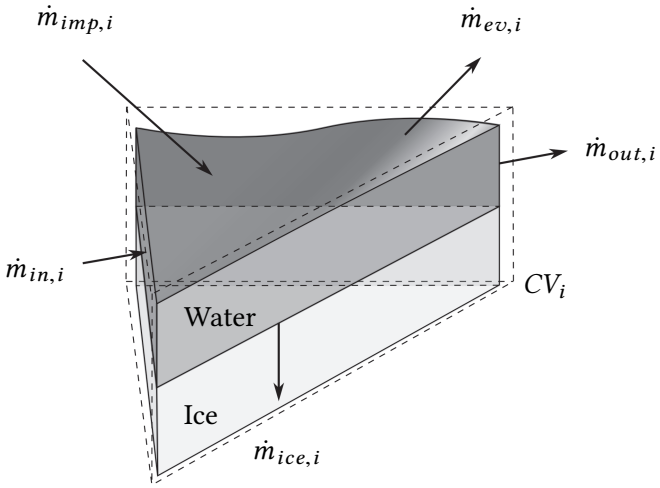

Figure 5.3: *Messinger control volume, 3D, mass flows*

VALIDATION FOR SUPERCOOLED LARGE DROPLET METHODS

6

The models described in the previous chapters have been implemented into the numerical method. Some models have been implemented in both the Lagrangian and Eulerian computational methods, while some models have only been implemented in the more advanced Eulerian method. Several validation tests have been performed to asses the suitability of these models for the prediction of ice accretion shapes involving SLD.

The results of each of the numerical methods is compared to the experimental data from Papadakis et al. [2007], who have defined a well-documented case including the details of the incoming droplet distributions, which are very important for an SLD catching efficiency calculation.

EXPERIMENTAL DATA 6.1

Data from several experiments was used to validate the numerical results. For a description of these experiments, see the following sections.

PAPADAKIS, NACA 23012 6.1.1

The paper from Papadakis et al. [2007] provides experimental data for a NACA 23012 airfoil. The asymmetrical profile was placed in NASA's icing wind-tunnel at Glenn Research Center, to study SLD effects. To this purpose several different droplet distributions were used, with an MVD in the range of 20 – 236 μm. For the present research, the largest MVD is of particular interest. As a reference, non-SLD, case the case with smallest MVD is used. The test conditions for these two cases are listed in Tab. 6.1, the measured droplet distributions are shown in Tab. 6.2 and Fig. 6.1.

The resulting ice accretion shapes obtained in the icing wind-tunnel are not known, but the resulting catching efficiencies are provided. Since the

Table 6.1: *Conditions for selected cases [Papadakis et al., 2007]*

	20 μm MVD	236 μm MVD
AoA	2.5°	
c	0.9144 m	
LWC	0.19 g/m^3	1.89 g/m^3
$\left\vert\vec{U}_{a,\infty}\right\vert$	78.23 m/s	
T_∞	299 K	
p_∞	101330 Pa	

catching efficiencies are only presented as a figure, numerical values have been obtained by tracing the provided figures, as shown in Appendix A. These catching efficiencies can be compared to the predicted catching efficiencies, removing the uncertainties and errors coming from the modeling of the ice accretion phase. The ice accretion modeling will be investigated in chapter 7.

A preliminary test showed that, although Papadakis et al. provide 27 and 10 bin droplet distributions, the 27 bin droplet distribution provides no noticeable increase in the accuracy of the numerical prediction. It does however cause a much longer simulation time. Therefore, the 10 bin droplet distributions are used throughout the validation process.

6.1.2 MDA - THREE ELEMENT AIRFOIL

A second source of experimental data comes from the Garteur project. This European project focused on ice accretion on multiple-element airfoils. A three element airfoil was provided (an airfoil with a leading edge slat and a trailing edge flap).

This geometry caused problems for the potential flow module of 2DFOIL-ICE so a modified geometry was created. limiting streamlines around the cove areas of the slat and main element were added to the geometry to avoid the appearance of multiple stagnation points on the airfoil sections.

The airfoil geometry is the same as that used by Vu et al. [2002], and the catching efficiencies from this report are used. The 10 bin droplet size

Table 6.2: *10-Bin droplet distributions for selected cases [Papadakis et al., 2007]*

Droplet bin	LWC [%]	Droplet size [μm] 20 μm MVD	236 μm MVD
1	5.0	3.850397	16.25037
2	10.0	9.390637	63.65823
3	20.0	13.80175	135.4827
4	30.0	19.60797	298.5197
5	20.0	25.4820	508.4572
6	10.0	30.73474	645.4684
7	3.0	35.19787	715.8689
8	1.0	38.32569	747.3936
9	0.5	40.66701	763.2455
10	0.5	44.36619	1046.767

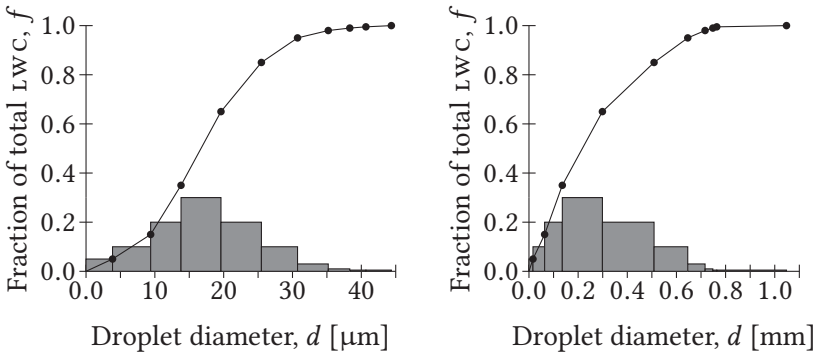

(a) 20 μm *MVD* ***(b)*** 236 μm *MVD*

Figure 6.1: *10-Bin droplet distributions for selected cases, individual bins (boxes) and cumulative (solid line) [Papadakis et al., 2007]*

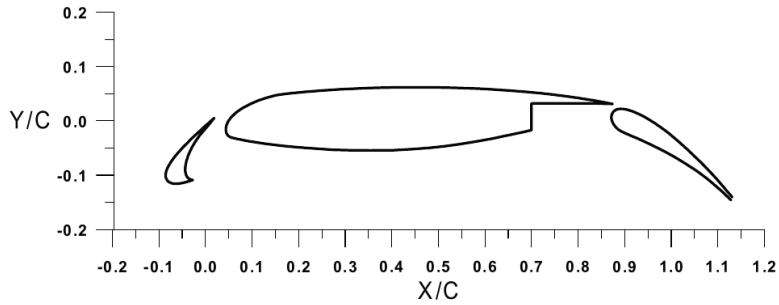

Figure 6.2: *MDA - three element airfoil, original geometry, picture from Vu et al. [2002]*

Table 6.3: *Conditions for selected cases [Vu et al., 2002]*

	21 µm MVD	92 µm MVD
AoA	4°	
c	0.9144 m	
LWC	0.22 g/m^3	0.21 g/m^3
$\left\vert\vec{U}_{a,\infty}\right\vert$	78.66 m/s	
T_∞	299 K	
p_∞	101330 Pa	

distributions from Sec. 6.1.1 are used. The remaining conditions are listed in Table 6.3.

6.2 COMPUTATIONAL DOMAINS

For comparison, a number of computational domains were used. The same domain, and corresponding computational grid, was used for as many cases as possible, to exclude effects of different grid sizes on the results.

6.2.1 TWO-DIMENSIONAL GEOMETRIES

The two-dimensional domains consist of two types, depending on the numerical method used. For the Lagrangian 2DFOIL-ICE method, only the

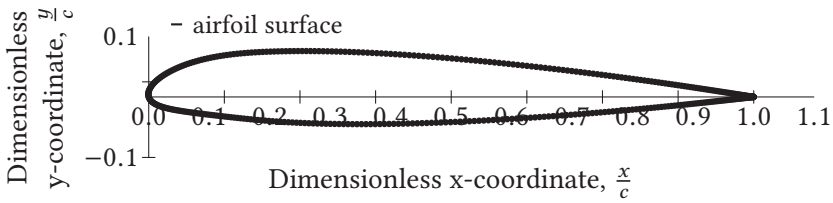

Figure 6.3: *2D NACA 23012 geometry, Lagrangian method*

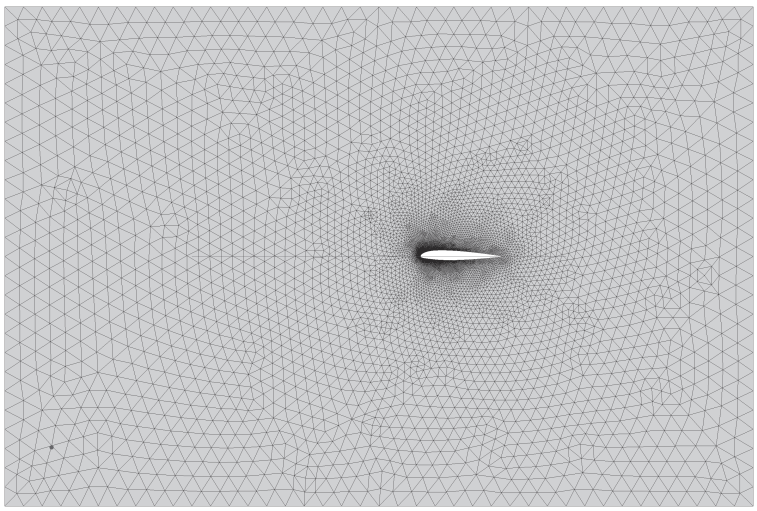

Figure 6.4: *2D NACA 23012 geometry, Eulerian method*

airfoil contour is discretized and modeled as line segments. For the Eulerian Droplerian method the entire domain is discretized as 2D surface elements.

NACA 23012

The NACA 23012 airfoil has been used in a number of analyses, the geometries used in these analysis are shown in Fig 6.3 and Fig. 6.4.

For the Lagrangian method, the computational domain consists of 400 contour elements. The panel distribution features a concentration of elements near the leading and trailing edge of the domain which is referred to as a double-cosine distribution. For the Eulerian domain 799 elements

Table 6.4: *2D NACA 23012, Eulerian grid parameters*

	Flow direction	Spanwise direction	Normal direction
Size	$-5c$, $+4c$	0	$-3c$, $+3c$
Vertices	42	0	28
Total vertices	14295	Airfoil surface vertices	799

Table 6.5: *2D MDA - three element airfoil, Eulerian grid parameters*

	Flow direction	Spanwise direction	Normal direction
Size	$-5c$, $+4c$	0	$-3c$, $+3c$
Vertices	21	0	14
Total vertices	9327	Airfoil surface vertices	7030

on the airfoil surface were used, and a total of 14295 triangular elements were used.

The domain of the Eulerian method is a finite domain, contrary to the Lagrangian infinite domain where the potential-flow solution is known at every point. The limits of the Eulerian domain are shown in Table 6.4.

MDA - THREE ELEMENT AIRFOIL

The three element airfoil is used by the Eulerian droplet trajectory method, combined with a potential-flow solution. The computational domain is shown in Fig. 6.5, this geometry includes the modifications needed to allow a potential flow solution for this complicated geometry.

The limits of the Eulerian domain are shown in Table 6.5.

6.2.2 THREE-DIMENSIONAL GEOMETRIES

Only the Eulerian method is used in three dimensions, so all domains are of the 3D grid type. The geometries are based on the above two-dimensional NACA 23012 geometry.

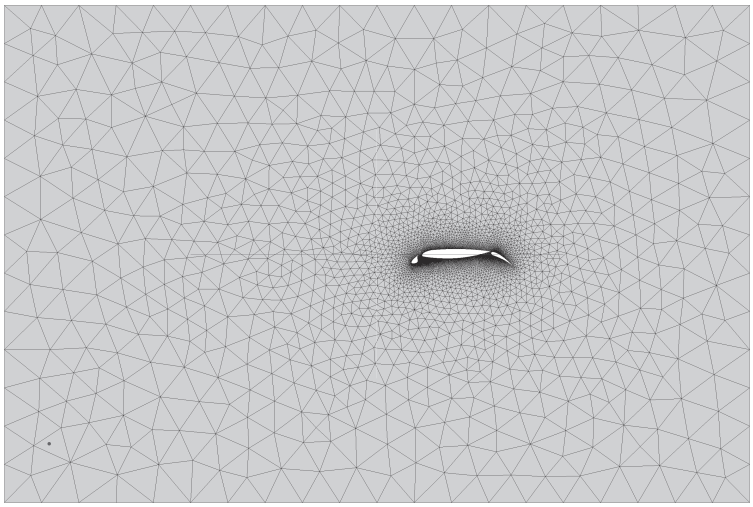

(a) *Overall view*

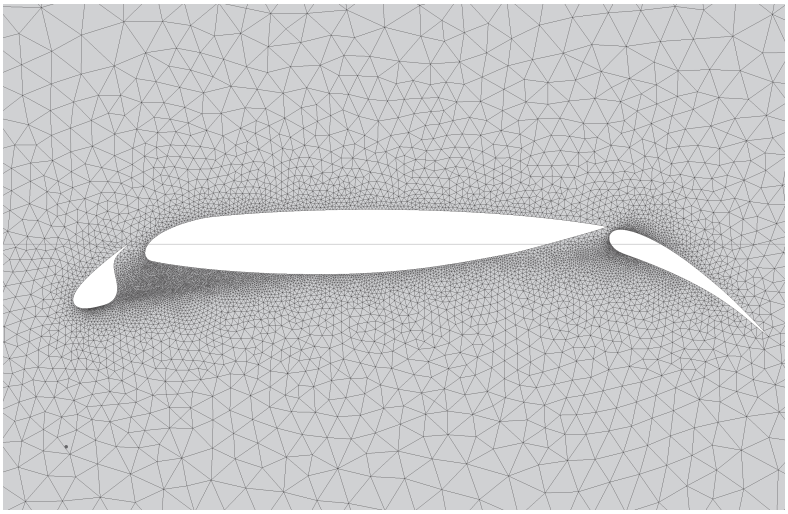

(b) *Airfoil view*

Figure 6.5: *2D MDA - three element airfoil geometry, Eulerian method*

Table 6.6: *Semi-2D NACA 23012, Eulerian grid parameters*

	Flow direction	Spanwise direction	Normal direction
Size	$-5c$, $+4c$	1 m	$-3c$, $+3c$
Vertices	42	3	28
Total vertices	166082	Airfoil surface vertices	56823

NACA 23012, SEMI-2D

This geometry is based on the 2D NACA 23012 geometry described in section 6.2.1. The basic geometry used is extruded into the third (span wise) dimension. This leads to a numerical grid described in Tab. 6.6

The root and tip of the so formed wing are modeled as wind-tunnel walls. A slip boundary condition is applied along the boundaries in the newly created third dimension to force the flow to align to the numerical domain and to render the domain effectively infinite in span wise direction.

The resulting three-dimensional geometry is shown in Fig. 6.6.

NACA 23012, SWEPT WING

The swept geometry is also based on the two-dimensional NACA 23012 geometry. However, it is now extruded using a base vector that is not perpendicular to the original 2D airfoil. The airfoil is extruded such that a wing with a 20° wing sweep is created.

The parameters from Tab. 6.6 are used. However, the wing is cut, halfway through the spanwise dimension. The *finite* swept wing is 0.5 m long with an abrupt "chopped off" wing tip. the walls in span wise direction are still applied using a slip boundary condition.

The resulting geometry is shown in Fig. 6.7.

6.3 MULTI-DISPERSE DROPLET DISTRIBUTION

One of the initial improvements made to both the Lagrangian and the Eulerian method is the inclusion of multi-disperse droplet distributions as explained in section 4.2.2. The effects of such a distribution versus a single droplet size are shown in Fig. 6.8. For the smaller droplet sizes

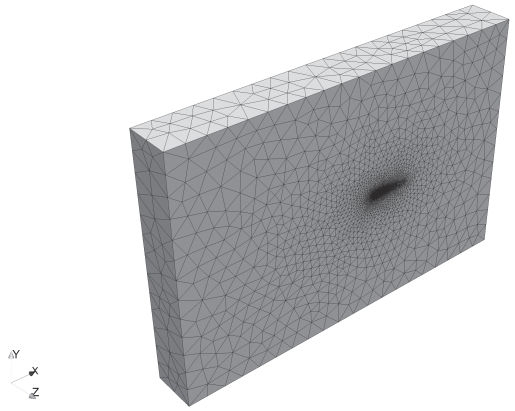

(a) *Side view*

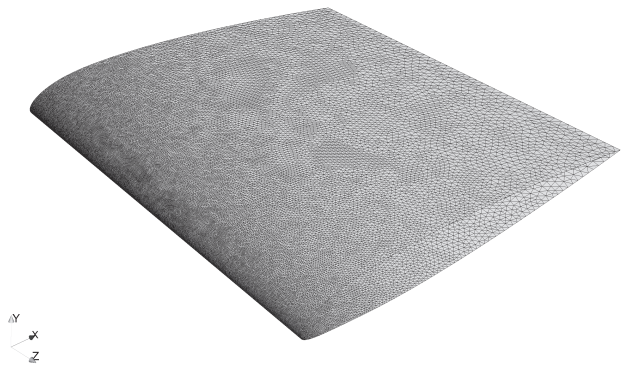

(b) *Internal view on the leading edge*

Figure 6.6: *Semi-2D NACA 23012 geometry*

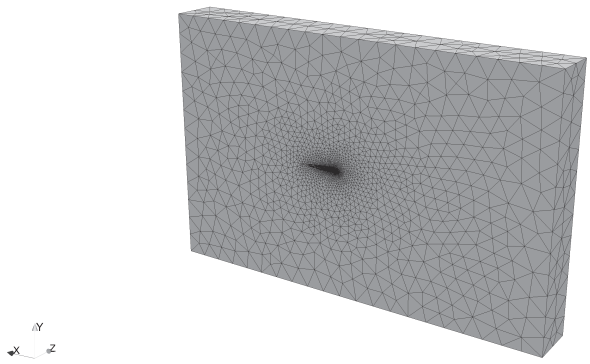

(a) *Side view*

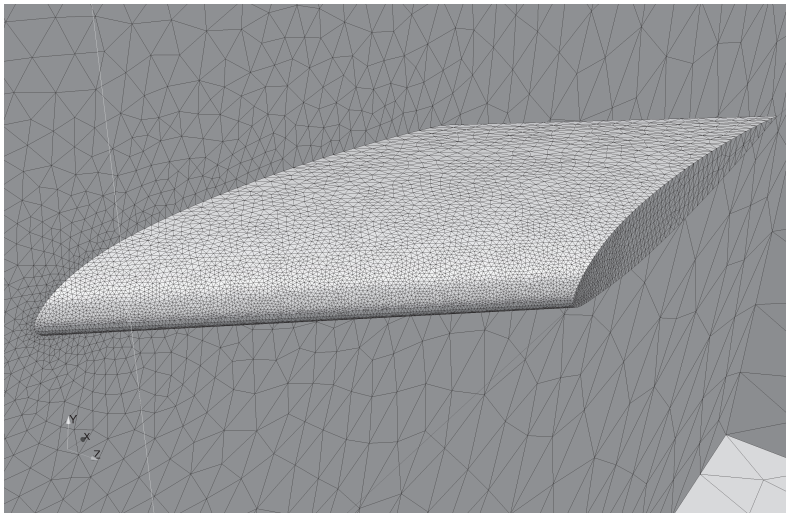

(b) *Internal view on the leading edge*

Figure 6.7: *Semi-2D swept NACA 23012 geometry*

a definite improvement is observed, instead of the sharp cutoff for the catching efficiency in Fig. 6.8(a) a more fluent result is found; which is in far better agreement with the experimental results. For the larger MVD this sharp cutoff was not found for the mono-disperse distribution, as seen in Fig. 6.8(b), so the improvement compared to the experimental results is less. For both the small and large MVD a slightly lower catching efficiency is obtained for the multi-disperse simulation, decreasing the over-prediction compared to the experimental results.

The accuracy can be estimated by looking at the integral of the catching efficiency

$$\beta_{total} = \frac{\int_{s=0}^{s} \beta \mathrm{d}s'}{s},$$

or in numerical form

$$\beta_{total} \approx \frac{\sum_{i=1}^{N_{panel}} \beta_i \left(\Delta s\right)_i}{s_{N_{panel}}}. \tag{6.1}$$

The total catching efficiencies are shown in Tab. 6.7. Though the improvement for the 236 μm MVD did not appear to be as large, when looking at the total catching effiency the improvement is actually much bigger than for the 20 μm MVD case.

LAGRANGIAN VS. EULERIAN 6.3.1

As a baseline, the multi-disperse calculations from both methods can be compared to see if the transition from the Lagrangian method to the Eulerian method does not introduce any artifacts. The results from both methods are shown in Fig. 6.9. Comparing the Lagrangian (2DFOIL-ICE) results with the Eulerian (Droplerian) results, only a small difference is found. This small difference is most likely due to numerical dissipation in the Eulerian method, overall the results are very similar.

DEFORMATION 6.4

The modified droplet drag-coefficient from Feo and Jarillo [2008] has been implemented. Equation 3.9 can be converted to a numerical relation in a straightforward fashion.

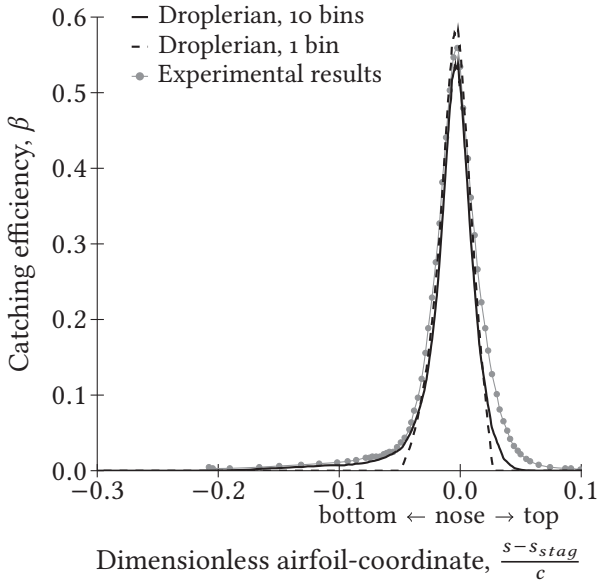

(a) 20 µm *MVD*

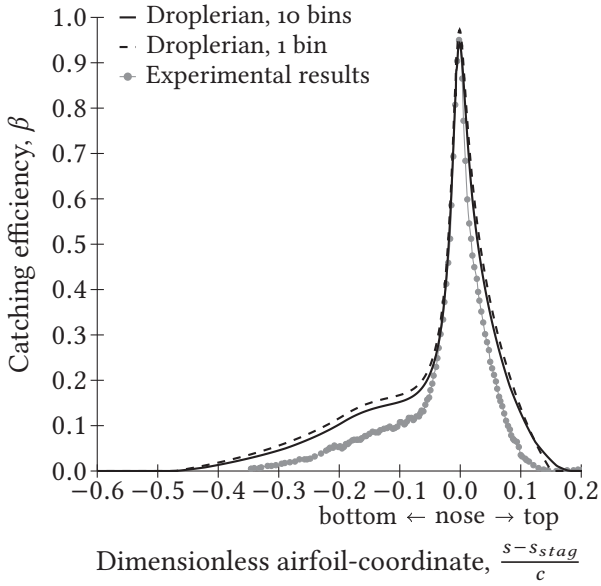

(b) 236 µm *MVD*

Figure 6.8: *Multi-disperse droplet distribution effects*

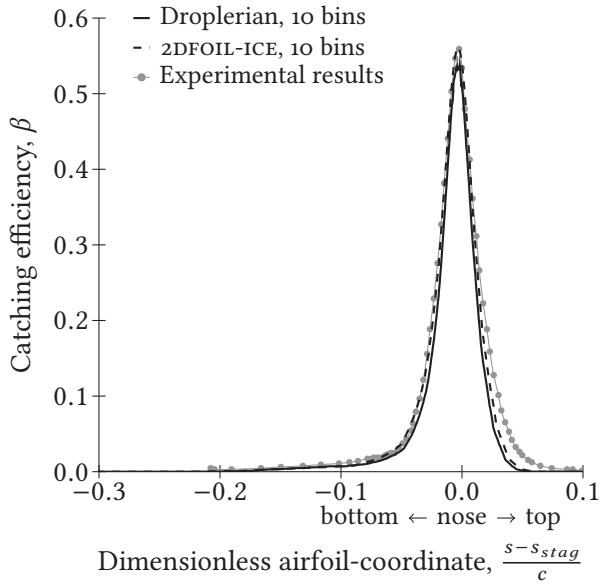

(a) 20 µm *MVD*

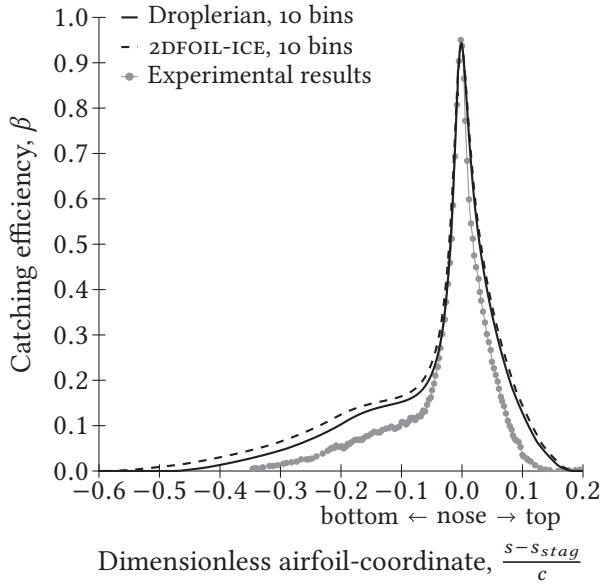

(b) 236 µm *MVD*

Figure 6.9: *Difference between Lagrangian and Eulerian results*

Table 6.7: *Total catching efficiencies for multi-disperse droplet distribution*

	β_{total} [−]	Δ exp. [%]	Improvement [%]
Experiment	0.012941614	–	–
1 Bin	0.010054046	−22.311670	–
10 Bins	0.010206984	−21.129902	1.1817679

(a) 20 µm *MVD*

	β_{total} [−]	Δ exp. [%]	Improvement [%]
Experiment	0.038614443	–	–
1 Bin	0.058026021	50.270251	–
10 Bins	0.053725100	39.132137	11.138114

(b) 236 µm *MVD*

Analyzing the impact of Eq. 3.9, the most important aspect is the threshold for droplet deformation: a minimum droplet Reynolds number of $\mathrm{Re}_d > 345$ is needed. This means that only for large magnitude of the relative droplet velocity $\left|\vec{U}_a - \vec{U}_d\right|$ a modification is implied. These high levels of relative droplet velocity are only encountered in the direct vicinity of an object in the flow. When a droplet is already this close to an object the modification due to the modified drag-coefficient has nearly no effect.

The impact of the deformation model is relatively moderate, but implementation is simple.

6.4.1 SINGLE ELEMENT AIRFOIL

The droplet deformation effect is tested on a single element airfoil, using the NACA 23012 data from Papadakis. Both the unmodified and modified droplet drag results are compared to the experimental catching efficiency results, as shown in Fig. 6.10 and Tab 6.8.

Based on Fig. 6.10(a) no visual change is notable due to the deformation model. This is because the model only has an effect for higher droplet diameters or higher Re_d. Looking at the value of β_{total} there is actually

Table 6.8: *Total catching efficiencies for multi-disperse droplet distribution with deformation*

	β_{total} [−]	Δ exp. [%]	Improvement [%]
Experiment	0.012941614	–	–
10 Bins	0.010206984	−21.129902	–
+ Deformation	0.010141722	−21.634188	−0.50428565

(a) 20 µm MVD

	β_{total} [−]	Δ exp. [%]	Improvement [%]
Experiment	0.038614443	–	–
10 Bins	0.053725100	39.132137	–
+ Deformation	0.052388102	35.669707	3.4624299

(b) 236 µm MVD

a 0.5% decrease in the prediction accuracy compared to the experimental value.

For the 236 µm MVD the shape slightly improves compared to the experimental results, especially on the upper side of the airfoil. This is supported by β_{total}, compared to the model without deformation a 3% improvement is observed.

THREE ELEMENT AIRFOIL 6.4.2

A more significant influence of SLD effects is expected for a multi-element airfoil; where larger relative velocities can be encountered in the wake of an airfoil segment, while the time before impact is still large. To asses this the MDA three element airfoil is used. The experimental catching efficiencies from Vu et al. [2002], described in Sec. 6.1.2 are used.

NON-SLD DIAMETER

First a non-SLD MVD is used as a general validation. The results for this 21 µm MVD are shown in Fig. 6.11. A minor difference between the modified

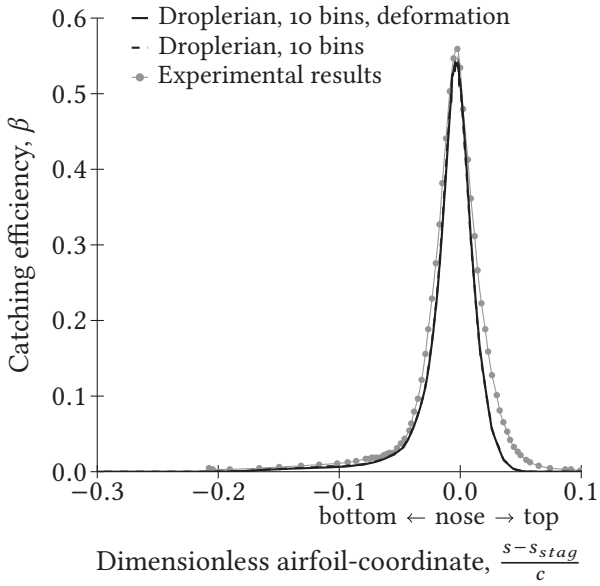

(a) 20 µm *MVD*

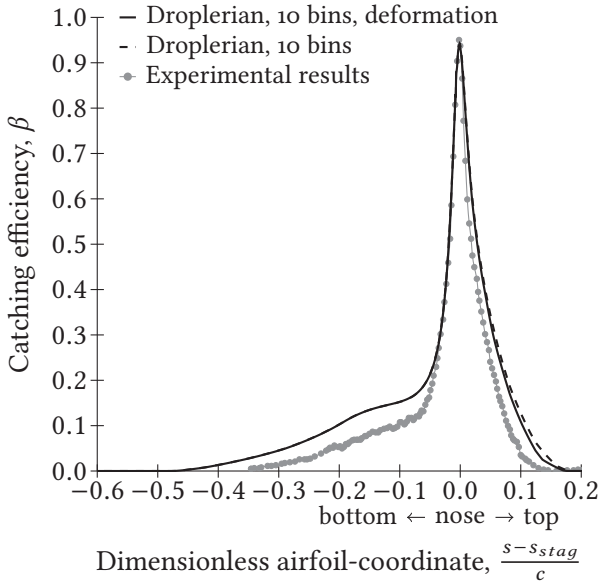

(b) 236 µm *MVD*

Figure 6.10: *Droplet deformation effect, single element airfoil*

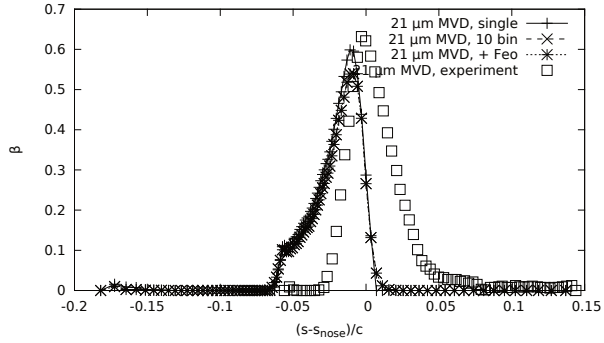

(a) slat

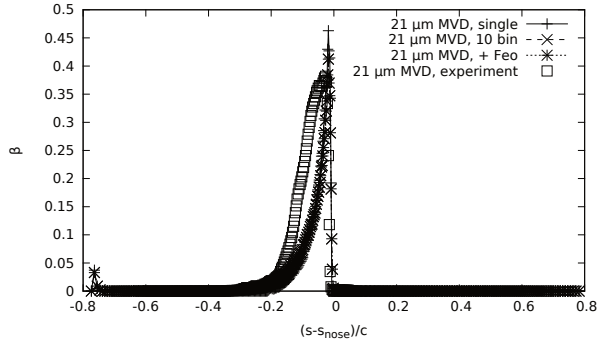

(b) main

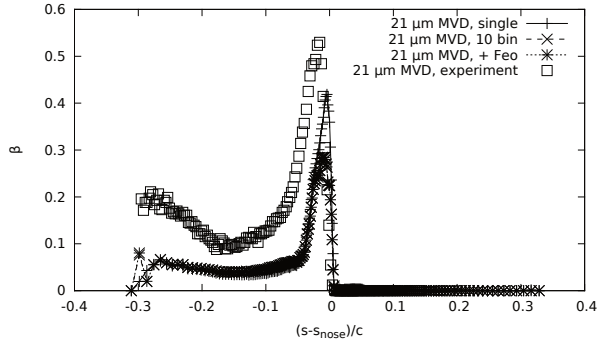

(c) flap

Figure 6.11: *Droplet deformation effect, three-element airfoil, small diameter droplets*

drag results and the spherical droplet drag results is visible. However, this difference is, for these non-SLD droplet diameter, negligible.

SLD DIAMETER

Second an SLD MVD is used. The results for this 21 μm MVD are shown in Fig. 6.12. For this larger, SLD sized MVD the difference between deformed droplet drag and spherical droplet drag. Especially the impingement on the main airfoil element differs a lot between the two drag models. This can be explained because this is also the area where droplets experience a large shear force, being transported through a very narrow flow section between slat and main element. The catching efficiency with the modified droplet drag relation is much closer to the experimental results than the result obtained with the spherical droplet drag relation.

6.5 SPLASHING

Splashing is thought to be a major SLD influence, so a large effect on the catching efficiency is expected, especially for the larger MVD. For the large droplet bins, no difference should be noted. Droplets impinging the surface are removed from the large bin, either with or without splashing model. However, with the splashing model, smaller secondary droplets are re-injected. This is shown in Fig.

Looking at the 20 μm MVD results in Fig. 6.13(a) (the dashed line), a clear loss of impinging mass is visible around the leading edge. This reduces the accuracy of the numerical model. This is caused by the limitation that the splashing model is valid for impact angles larger than 4°. The total catching efficiency is decreased by 6%, as shown in Tab. 6.9.

For the 236 μm MVD the splashing model does lead to an improvement in accuracy compared to the experimental values, as shown in Fig. 6.13(b). Again a decrease of the catching efficiency is observed near the leading edge, but this does not have as great an effect as for the small MVD case. The improvement comes from the areas downstream of the leading edge, where the catching efficiency is reduced to values that are in better agreement to the experiments. Table 6.9 shows an improvement in total catching efficiency of 25%.

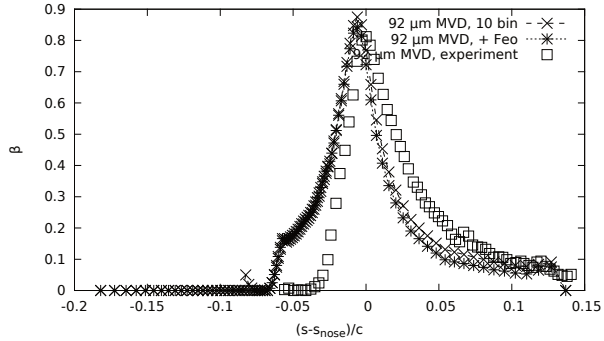

(a) *slat*

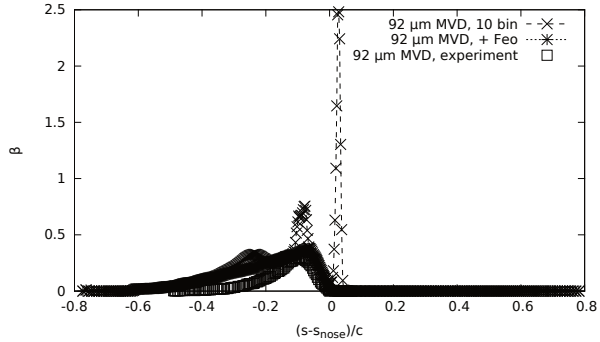

(b) *main*

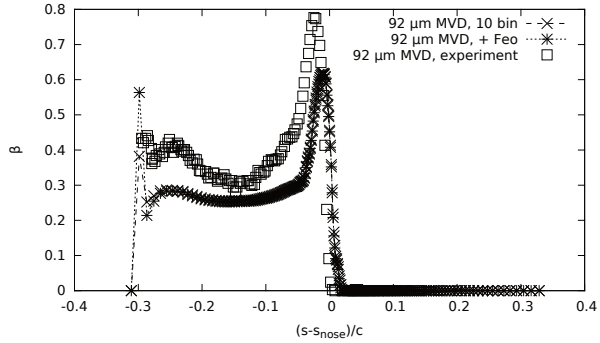

(c) *flap*

Figure 6.12: *Droplet deformation effect, three-element airfoil, large diameter droplets*

Table 6.9: *Total catching efficiencies for multi-disperse droplet distribution with splashing*

	β_{total} [−]	Δ exp. [%]	Improvement [%]
Experiment	0.012941614	–	–
10 Bins	0.010206984	−21.129902	–
+ Splash	0.0094145110	−27.253403	−6.1235012

(a) 20 µm MVD

	β_{total} [−]	Δ exp. [%]	Improvement [%]
Experiment	0.038614443	–	–
10 Bins	0.053725100	39.132137	–
+ Splash	0.043845866	13.547840	25.584296

(b) 236 µm MVD

It is interesting to note that, although re-impingement is implicitly possible in the current method, apparently no re-impingement takes place with the splashing model active. Figure 6.13 shows that the catching efficiency resulting from the splashing simulation is always smaller or equal to the catching efficiency without the splashing model, as is the total catching efficiency in Tab. 6.9.

6.6 REBOUND

The splashing model provided (for the large MVD) a big improvement, however; for the areas furthest downstream of the leading edge, an over-prediction of the catching efficiency is still found. Physically, these regions, near the impingement limits, are the regions where rebound occurs. Therefore, a rebound model could potentially improve the catching efficiencies even further.

For the small 20 µm MVD case, the splashing model proved a decrease in numerical model accuracy. The rebound model only deteriorates the comparison with the experiment, the catching efficiency near the leading

Table 6.10: *Total catching efficiencies for multi-disperse droplet distribution with splashing and rebound*

	β_{total} [−]	Δ exp. [%]	Improvement [%]
Experiment	0.012941614	–	–
10 Bins	0.010206984	−21.129902	–
+ Splash + Reb.	0.0085830681	−33.679022	−12.548120

(a) 20 µm MVD

	β_{total} [−]	Δ exp. [%]	Improvement [%]
Experiment	0.038614443	–	–
10 Bins	0.053725100	39.132137	–
+ Splash + Reb.	0.039413463	2.0692270	37.062910

(b) 236 µm MVD

edge is further decreased as shown in Fig. 6.13(a). This leads to a further decrease of 6% in β_{total}, to a total deficit of 12% compared to the experimental value, shown in Tab. 6.10.

The larger 236 µm MVD does improve from the inclusion of a rebound model, as seen in Fig. 6.13(b). A total improvement of 37% in β_{total} is found, leading to a difference with the experiment of only 2% (Tab. 6.10).

While the splashing model did not show evidence of any re-impingement of secondary droplets, the rebound model does show some re-impingement. For Fig. 6.13(b), an increase in the catching efficiency with rebound model is visible in the area around $s = -0.2$. The total catching efficiency however is still reduced, compared to the splashing model it is even reduced further, as shown in Tab. 6.10.

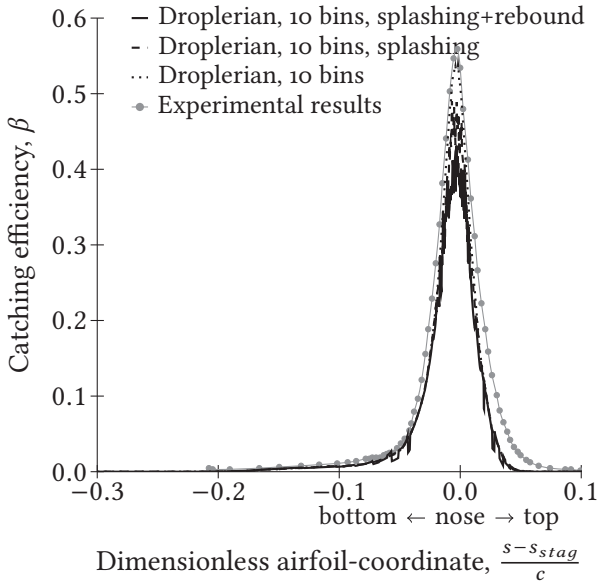

(a) 20 µm *MVD*

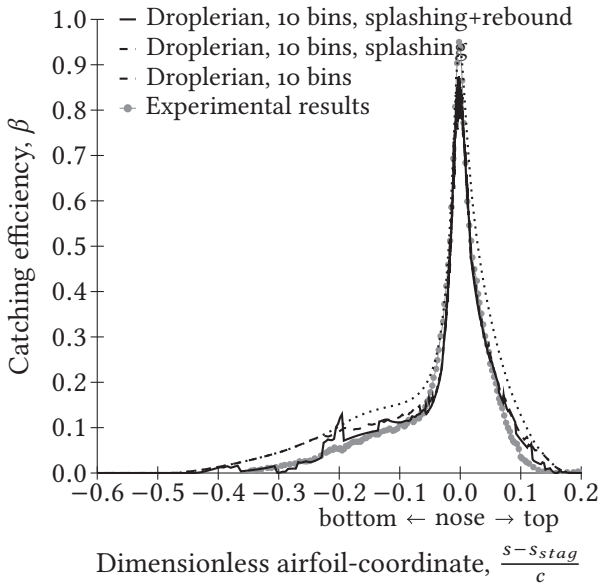

(b) 236 µm *MVD*

Figure 6.13: *Splashing and rebound effect*

THREE-DIMENSIONAL 6.7

The extended numerical model was validated, first against the existing 2D model, with results and experiments readily available; and second, against the three-dimensional experiments from the EXTICE project.

COMPARISON TO TWO-DIMENSIONAL METHOD 6.7.1

A number of tests were performed to compare the accuracy of the newly created 3D numerical ice accretion model to that of the original 2D model. The most basic assessment can be made by judging flow patterns across the airfoil surface. Second, catching efficiencies can be compared to true two-dimensional results. Third the effect of three dimensional wing on the catching efficiency results can be determined.

SEMI-2D WING SECTION

The model used for this validation test consists of a three-dimensional extrusion of a 2D NACA 23012 profile. A triangular surface mesh was formed on the airfoil surface, which was consequently used to form a three-dimensional tetragonal mesh, as described in Hospers [2007]. Using the resulting geometry shown in Fig. 6.6 an assessment of the flow patterns across the airfoil surface was performed.

The conditions defined in section 6.1.1 are used to define this 3D case as well, leading to results comparable with the 2D results from section 6.3.

Figure 6.14 shows that the method defined in section 5.1 provides a flow pattern that may be expected; surface liquid will flow from leading-edge to trailing edge, both on the top and bottom of the airfoil. As expected, the flow is essentialy 2D, no flow in longitudinal (root to tip) direction is visible.

The catching efficiency can be shown in three dimensions as indicated in Fig. 6.15. Again, little variation in longitudinal direction is observed. Plotting the catching efficiency in every surface element as a function of the airfoil s-coordinate, gives a catching efficiency curve, similar to those for the 2D profiles. A direct comparison is made in Fig. 6.16.

The 3D catching efficiency tends to be slightly lower than the 2D values. This may be due to the fact that incoming droplets are dissipated in 3D

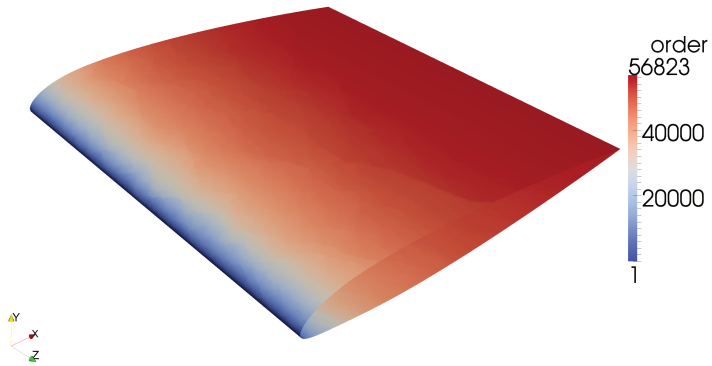

(a) *Order of airfoil surface elements*

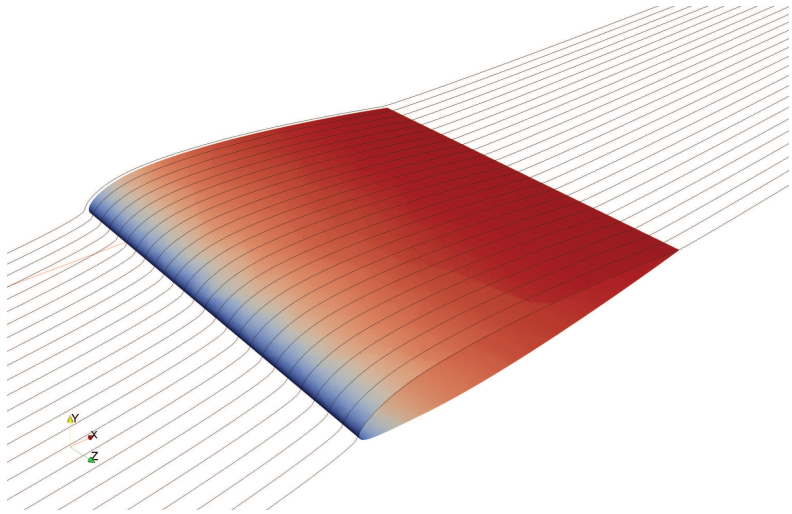

(b) *Order with streamlines along the surface, showing surface flow direction*

Figure 6.14: *Extruded semi-2D geometry*

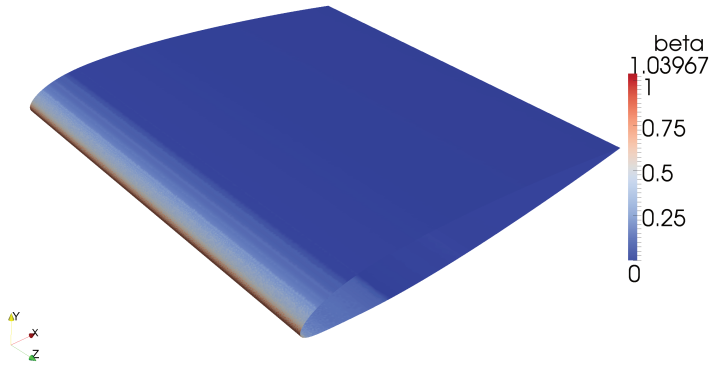

Figure 6.15: *Three-dimensional catching efficiency results*

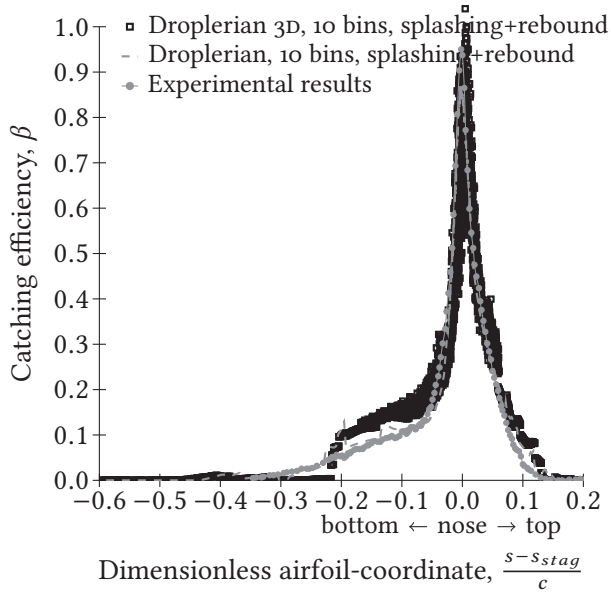

Figure 6.16: *Catching efficiency for three-dimensional results, projected to two dimensions, semi-infinite wing*

Table 6.11: *Total catching efficiencies for swept 3D wing*

	β_{total} [−]	Δ exp. [%]	Change [%]
Experiment	0.038614443	–	–
2D	0.039413463	2.0692270	37.062910
Semi-2D	0.038586636	6.0694054	3.9190849
Swept	0.035240569	−4.7144608	−10.166802

directions, but possibly this is due to numerical dissipation. In general, the results for the 2D and 3D models is very comparable, especially considering the fact that the semi-2D wing results are slightly influenced by the boundaries of numerical domain.

SWEPT WING SECTION

A natural extension is towards a swept wing. Comparison to the 2D method is less meaningful, however, a visual inspection of the surface flow pattern may provide insight into the correctness of the numerical model.

Figure 6.17 shows the flow pattern expressed again in terms of the surface element order. The surface flow originates from the wing root, and flows simultaneously towards the trailing-edge and towards the wing tip. This proves that the method is capable of predicting a surface flow pattern that is multi-dimensional; 2D in fact, from a stagnation line across the surface. This is in contrast to the flow patter from a pure two-dimensional method, which only predicts flow from the stagnation point towards the trailing-edge; an essentially 1D flow.

It is no longer useful to plot the catching efficiency in two dimensions. However a 3D plot can be made, as shown in Fig. 6.18. The catching efficiency is notably lower, due to the a flow component around the wing tip as can been seen in Fig. 6.17(b). However, a comparison based on the integrated β_{total} from Eq. 6.1 can be made. The comparison is shown in Tab. 6.11. A decrease of 10% in β_{total} is observed in going from a straight to a swept wing.

The most significant 3D effect is observed in the mass of surface (or runback) water entering each surface element, $m_{c,in}$. The spanwise component

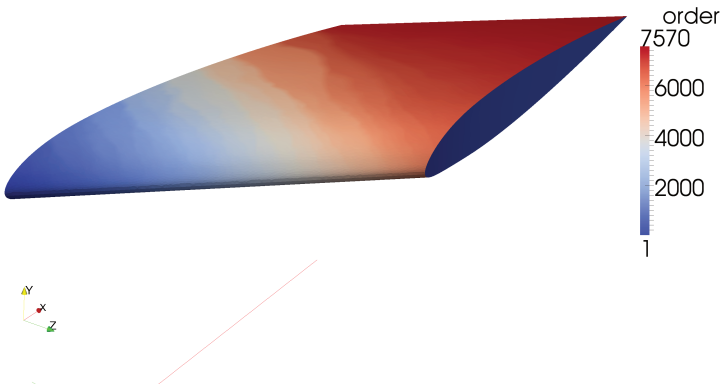

(a) *Order of airfoil surface elements*

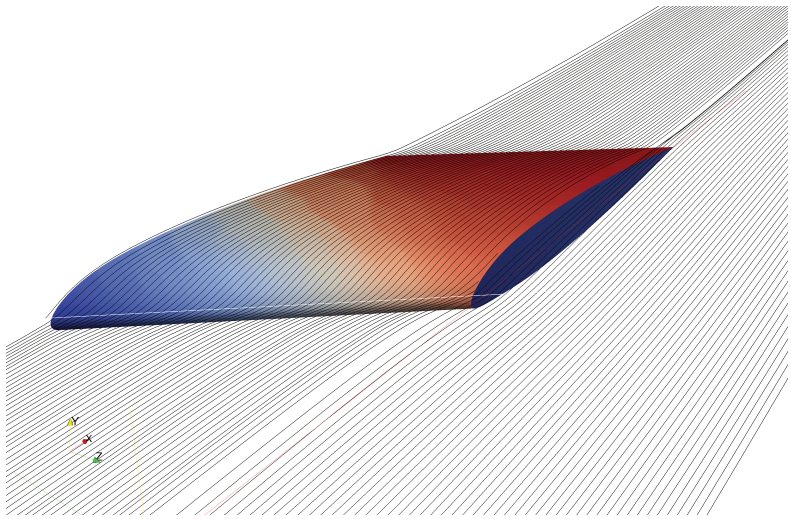

(b) *Order with streamlines along the surface, showing surface flow direction*

Figure 6.17: *Extruded swept geometry*

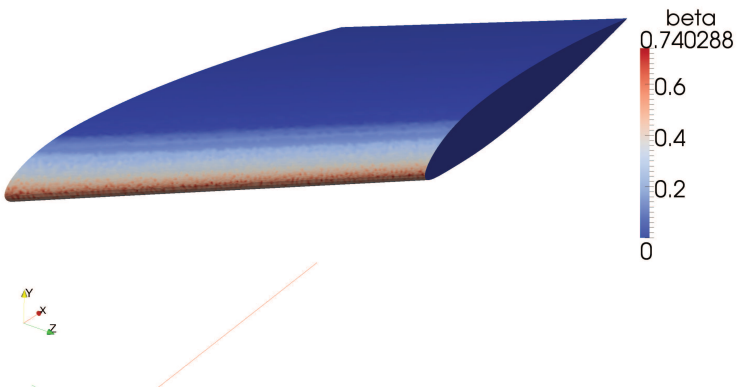

Figure 6.18: *Three-dimensional catching efficiency results, swept 3D wing*

of the surface flow pushes surfaces water towards the wing tip. This is shown in Fig. 6.19.

6.8 CONCLUSION

All models appear to have a beneficial influence on the predicted catching efficiencies. However, it is very hard to quantify the improvement since the catching efficiency depends on a large number of (partially unknown) parameters, e.g., splashing appears to have larger improving influence for large droplets, while it may have a deteriorating influence for non-SLD diameters.

A ranking can be made from largest to smallest influence based on the results from this chapter:

1. multi-disperse droplet diameters,
2. splashing,
3. deformation,
4. rebound.

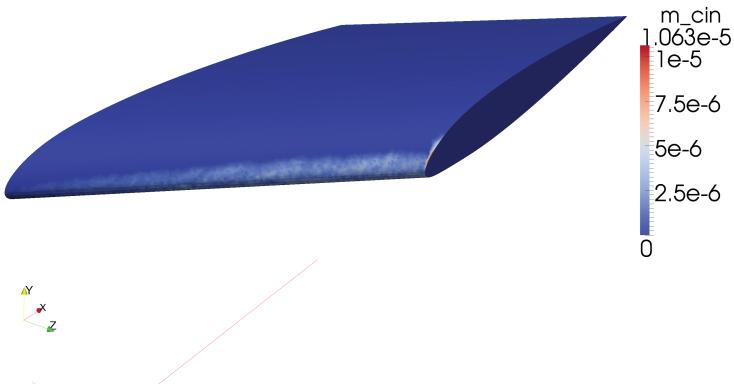

Figure 6.19: *Three dimensional surface mass flow, $m_{c,in}$, results*

VALIDATION OF ICE ACCRETION METHOD

7

The models described in the previous chapters have been implemented into the numerical method. Some models have been implemented in both the Lagrangian and Eulerian codes, while some models have only been implemented in the more advanced Eulerian method. Several validation tests have been performed to asses the suitability of these models.

Each of the numerical methods is compared to the experimental data from Papadakis et al. [2007], who have defined a clear case including the incoming droplet distributions, which are very important for an SLD catching efficiency calculation.

EXPERIMENTAL DATA 7.1

Several experiments were used to validate the numerical data. For a description of these experiments, see the following sections.

EXTICE, CEPR - NACA 0012 7.1.1

Within the scope of the EXTICE project a validation experiment was conducted in the DGA CEPr (Centre d'Essais de Propulsion) facilities. These facilities include a small scale icing wind tunnel, with advanced spray injection possibilities.

Catching efficiencies and ice accretion shapes were determined for a straight, semi-infinite, NACA 0012 airfoil geometry.

Cloud validation studies were performed, rendering some interesting ice shapes, suitable for comparison to the computational methods. These ice shapes were formed from specific droplet clouds, representing the droplet distributions found in SLD clouds. These distributions are shown in Fig. 7.1. The tabular distributions consist of 40 droplet bins.

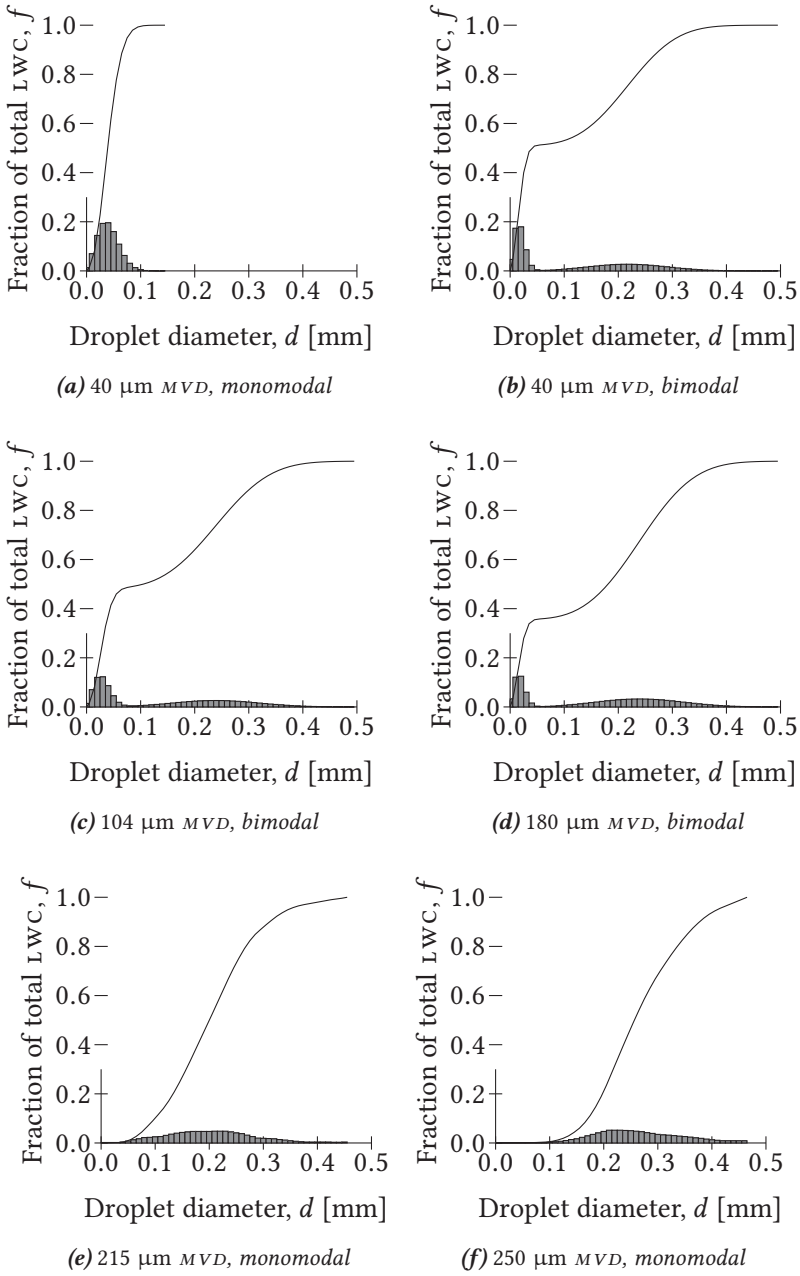

(a) 40 µm *MVD, monomodal*

(b) 40 µm *MVD, bimodal*

(c) 104 µm *MVD, bimodal*

(d) 180 µm *MVD, bimodal*

(e) 215 µm *MVD, monomodal*

(f) 250 µm *MVD, monomodal*

Figure 7.1: *Droplet distributions in CEPR experiments*

Table 7.1: *Selected CEPR cases*

case	Mach	T °C	altitude m	MVD	LWC g/m^3	AoA °	time s
E5	0.2	−25	0	(b)	0.3	2	450
E7	0.2	−10	0	(b)	0.3	2	450
E19	0.2	−25	0	(e)	0.22	2	616

Figures 7.1(b–d) show the typical bimodal droplet distributions encountered in SLD clouds. Distributions (e) and (f) were added to the initial test matrix because preliminary CFD results showed an increased possibility of SLD phenomena, to ensure that SLD models could be validated.

The EXTICE campaign contained 22 cases numbered E1–E22. Each distribution from Fig. 7.1 was used at least once, generally in a catching efficiency run combined with one or more ice accretion runs.

Catching efficiencies are determined by running an ice accretion test at −25 °C and calculating impingement from measured ice thickness, under the assumption that all water freezes instantly. The ice accretion runs vary in simulated temperature, altitude, speed and duration.

From these 22 runs, three cases were selected. Many cases are outside of the considered scope because the Mach number for these cases is too high, either 0.5 or 0.65 From the selected cases one case is at 40 µm MVD, and one case is at 215 µm MVD. This corresponds with distributions (b) and (e) from Fig. 7.1 and with cases E5, E7, and E19 from the CEPR EXTICE campaign respectively. The selected cases are shown in Tab. 7.1.

Part of this work was also used by Norde [2013] to validate an extended surface flow model.

EXTICE, DASSAULT - THREE ELEMENT SWEPT WING 7.1.2

The EXTICE project pertained not only the previously mentioned CEPR tests, but also an extended test in the CIRA wind tunnel. This wind tunnel is one of the largest icing wind tunnels in the world, allowing for a cold and depressurized atmosphere. The model used in the EXTICE tests was provided by the Dassault Aviation company, a partner in the project. They provided a 3D wing used on their Falcon aircraft , with a wing sweep and adjustable slat and flap.

Photograph by bagalute on flickr, available under a CC BY 2.0 license

Figure 7.2: *Photograph of a Dassault Falcon 2000, Deutsche Telekom D-BONN, with a wing very similar to the EXTICE model*

Table 7.2: *Selected CIRA case*

run	Mach	T °C	altitude m	MVD	LWC g/m^3	AoA °	time s
12	0.183	−5	0	165.33	0.65	−2	457

The flap was fixed during the tests, at an angle chosen to minimize wind tunnel wall effects. Configurations with and without slat deflection were tested. The CIRA wind tunnel allowed for a scale of the wing geometry of 1:2.

From the test matrix run 12 was chosen as a test case for the 3D numerical ice accretion model. This case is particularly suited because of its high bi-modal droplet distribution and neutral angle of attack, for which a geometry was made available by Dassault Aviation in the EXTICE project.

CIRA defined two sections for which an ice accretion was traced. The location of these sections were defined and measured from the tip end of the slat. Both sections were traced as two-dimensional sections perpendicular

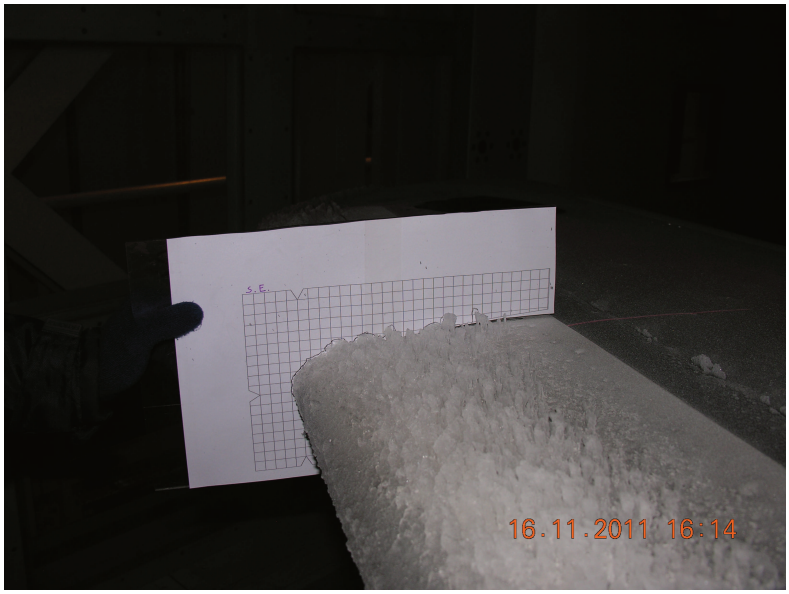

Figure 7.3: *Photograph of the traced ice shape on the tip section of the Dassault wing, picture from* CIRA

to the leading edge, as demonstrated in Fig. 7.3. A root and tip section are defined, measured at 53.5 cm and 161.1 cm from the slat tip respectively.

COMPUTATIONAL DOMAINS 7.2

The two-dimensional ice accretions are validated using the geometry from section 7.1.1. However, the three-dimensional results are based on a new three-dimensional geometry.

DASSAULT - THREE ELEMENT WING SECTION 7.2.1

The basic geometry for this computational analysis was kindly provided by Dassault Aviation in the Extice project. A fully three-dimensional CAD file was provided, including CIRA wind tunnel section. This model was not completely suited for a CFD analysis, so some model cleanup was

Table 7.3: *3D Dassault wing, Eulerian grid parameters*

	Flow direction	Span direction	Normal direction
Size	−4500, +3800 mm	2390 mm	−1800, +1800 mm
Vertices	22	7	10
Total vertices	89205	Airfoil surface vertices	36431

performed: closing of geometry sections and smoothing of abrupt geometric orientations. The final model is shown in Fig. 7.4.

The computational model has a root chord length, including the (retracted) slat and flap, of 1808 mm. The wing half span is 3190 mm. The sweep angle measured along the leading edge is 32.3°. Details on the numerical domain are given in Table 7.3

7.3 TWO-DIMENSIONAL ICE ACCRETIONS

The NACA 0012 airfoil is not an airfoil that creates specific high shear in the surrounding fluid flow, nor is it inherently three-dimensional. However, it provides a good case for basic testing of the splashing and rebound model, without introducing complicating SLD physics.

7.3.1 ICE ACCRETION SHAPES

For each of the selected cases an ice accretion shape was computed. They are shown and analyzed in the following sections.

CASE E5

Case E5 is a base case at non-SLD conditions. Droplerian should perform well here as no additional changes to the original models have been implemented. The ice accretion shape is good compared to the experimental shape.

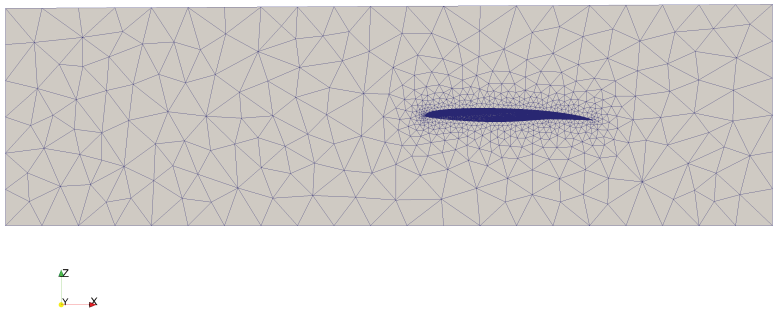

(a) *Side view*

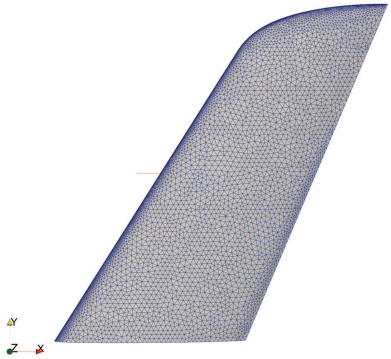

(b) *Internal top view of the wing*

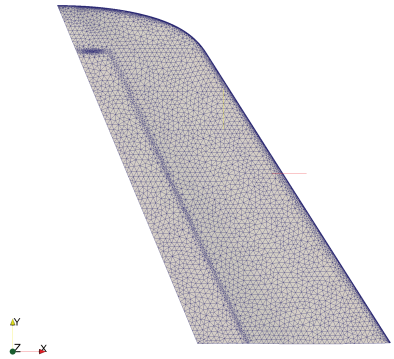

(c) *Internal bottom view of the wing*

Figure 7.4: *3D Dassault wing, modified geometry*

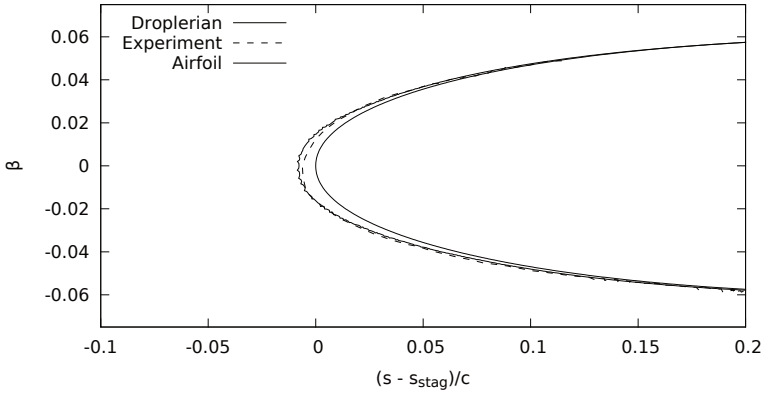

Figure 7.5: *Ice accretion shape result for case E5*

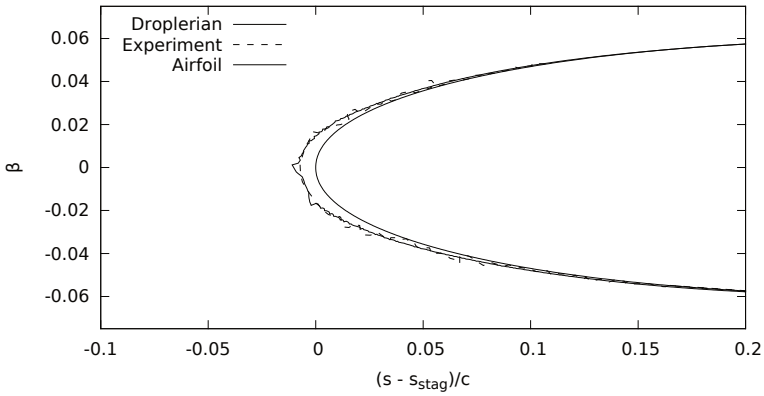

Figure 7.6: *Ice accretion shape result for case E5*

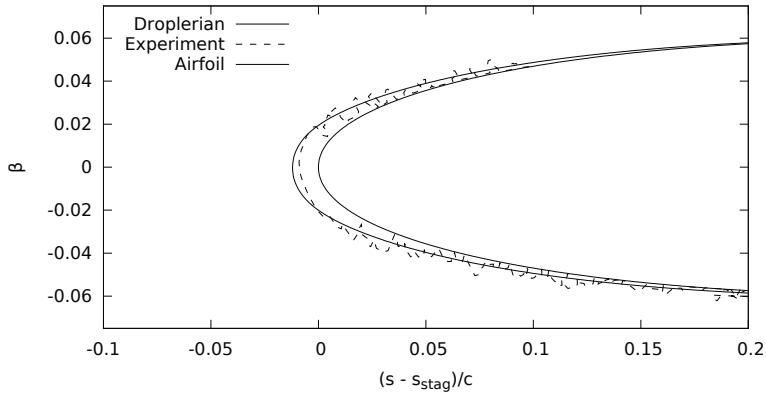

Figure 7.7: *Ice accretion shape result for case E19*

CASE E7

Case E7 is based on case E5 but with a higher temperature. This will create a different type of ice accretion, with more of a rime-ice shape, since not all of the deposited water will freeze immediately.

Again the results are good, however micro-features of the ice accretion are not caught by the numerical model.

CASE E19

Case E19 is a true SLD case. At 215 µm MVD this is a test case for the splashing and rebound models. The results are exceptional, a good agreement to the experimental ice accretion shape is found. However, again, a lack of micro-features of the accretion is to be noted.

CONCLUSION 7.3.2

In two dimensions the ice accretion shapes agree with the experimental ice accretion shapes. No greater difference is observed for SLD and non-SLD conditions. A discrepancy for both conditions is the lack of micro-features for the numerical ice accretion shape.

7.4 THREE-DIMENSIONAL ICE ACCRETIONS

Three-dimensional ice accretions are validated using the CIRA experiments and Dassault geometry described in sections 7.1.2 and 7.2.1, respectively.

CIRA defined two cut planes for which an ice accretion shape was traced. These sections are extracted from the simulation results as well, to compare with the experimental results.

7.4.1 CATCHING EFFICIENCY

The catching efficiency is largest along the leading edge. What draws attention here is a second impingement region downstream of the leading edge on both the top and bottom of the airfoil surface. These impingements are hard to see, but are present none the less.

Three-dimensional effects are visible around the wing tip, where the impingement area moves along with the wing edge.

7.4.2 ICE ACCRETION SHAPE

The ice accretions are shown in Fig. 7.10, in grayscale on a blue wing surface. A white color means a (thin) layer of ice is present. A thin layer of ice along the bottom of the airfoil is visible, especially near the flap. There is also a small amount of impingement here, although not visible in the figures in the previous section.

Note also a secondary impingement region on the top of the airfoil, downstream of the leading edge. This ridge is also visible on photographs of the experiments in Fig. 7.11. Note that the experimental ice accretions show a larger effect of the wind tunnel wall near the root of the section, see Fig. 7.11(b). This can be explained by the lack of viscosity in the flow model used in the simulated flow field for the numerical model.

For the section ice accretions a more quantitative conclusion can be drawn. The ice accretion thicknesses for both the sections are predicted fairly accurate close to the leading edge. However, downstream of the leading edge, the ice accretion thickness is underestimated. This is due to the presence of horn like shapes in the experiment, as seen in photographs, which are not reproduced by the numerical model. The total mass of ice predicted by the model is most likely similar to the mass in the experiment.

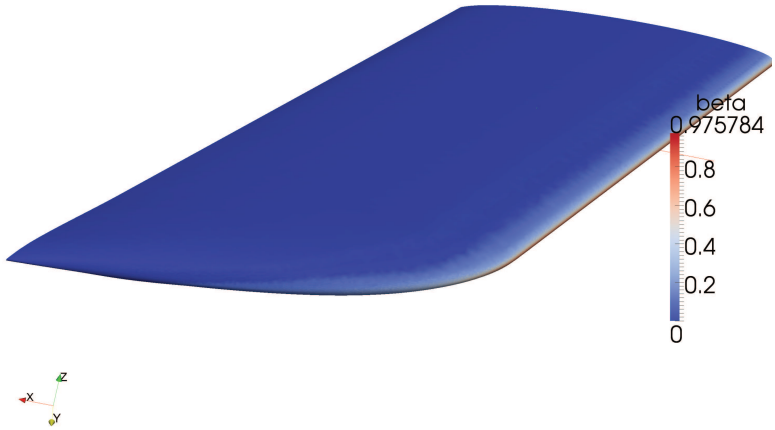

(a) Top view

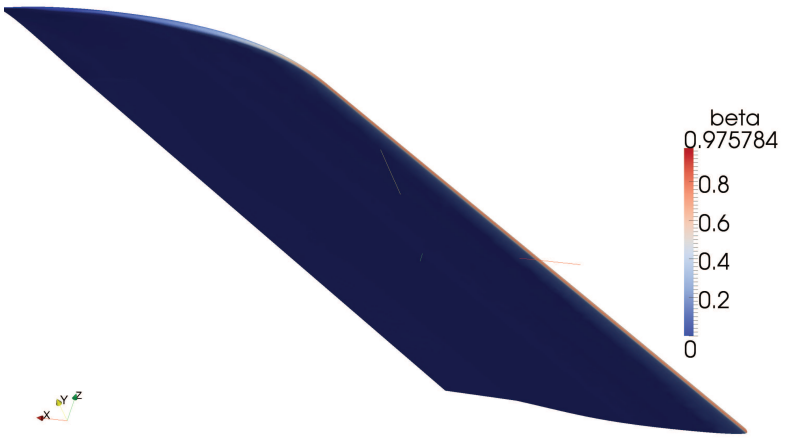

(b) Bottom view

Figure 7.8: *Catching efficiency results, β*

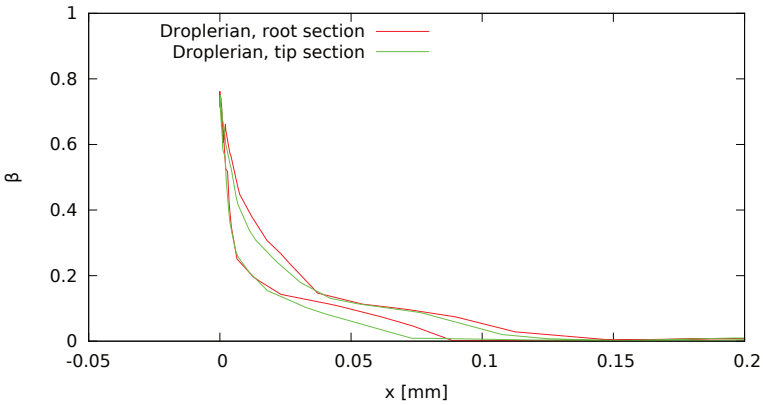

Figure 7.9: *Catching efficiency results, Dassault wing, measured from the wing leading edge*

However, due to a more sparse distribution of ice on the airfoil surface the horns grow to a thicker, more erratic ice layer.

7.4.3 CONCLUSION

Data shows that the numerical model is fairly accurate. The largest imbalance between numerical and experimental results is found in the micro-features of the ice accretions, such as horns or ridges. These micro-features are not captured by the numerical model and, as such, the prediction of thickness and shapes of ice accretions is different to what is seen in experiments.

The CIRA results indicate a maximum ice accretion thickness of 13.1 mm, while the numerical model predicts a maximum ice thickness of 11.7 mm. This gives an error of −10.7%.

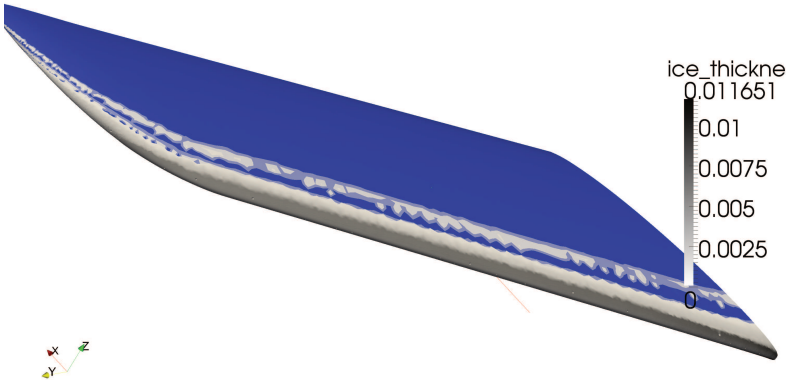

(a) *Top view*

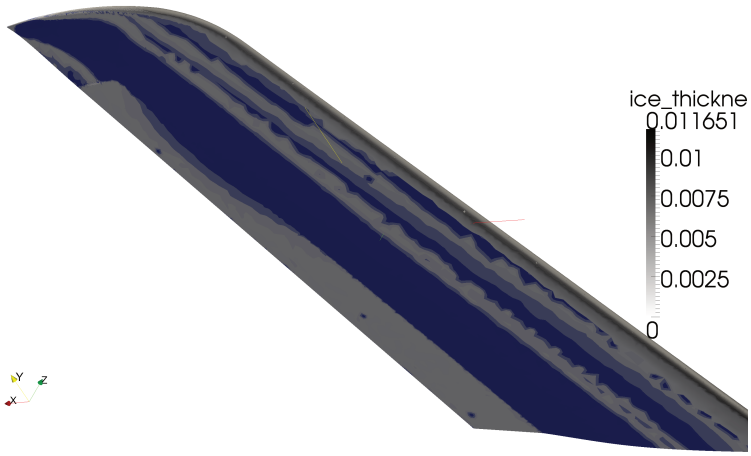

(b) *Bottom view*

Figure 7.10: *Ice accretion shape result, Dassault wing, thickness in* mm

(a) *Front view*

(b) *View on traced sections from the wing root*

Figure 7.11: *Photographs showing experimental ice accretions on the Dassault wing, picture from* CIRA

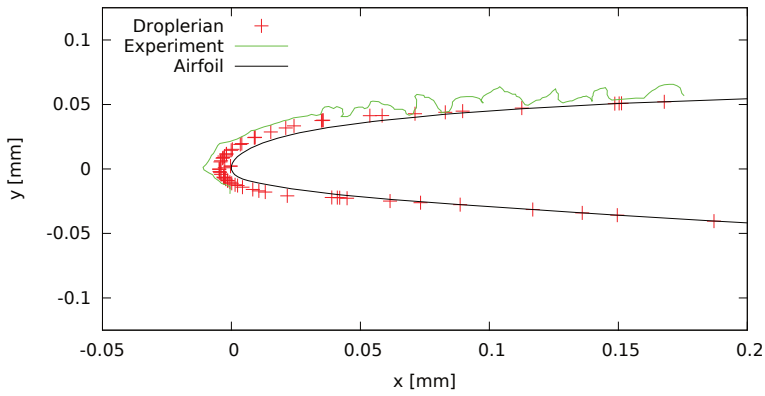

(a) Root section

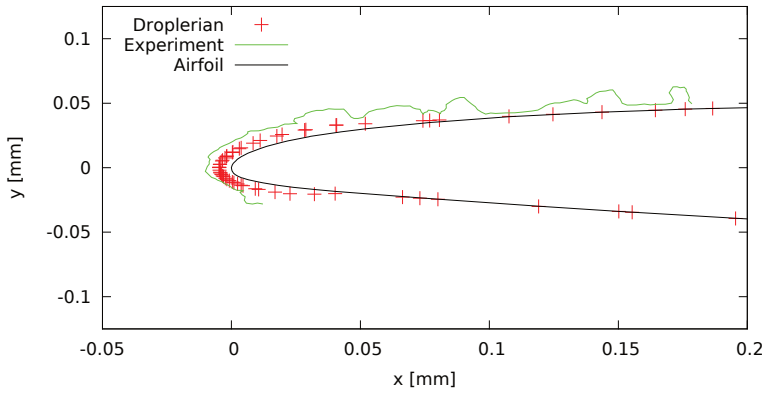

(b) Tip section

Figure 7.12: *Ice accretion shape result, Dassault wing, thickness in* mm

CONCLUSIONS AND RECOMMENDATIONS 8

BASED ON THE RESEARCH RESULTS described in this thesis the following conclusions and recommendations are given.

CONCLUSIONS 8.1

Based on the validation results for both the catching efficiency in chapter 6 and the ice accretion shapes in chapter 7, for both two-dimensional and three-dimensional geometries, the following can be concluded:

- The main force components determining the droplet trajectories for both non-SLD and SLD are:
  - (deformed) droplet drag,
  - history force $\left(< 0.1 \cdot F_{drag}\right)$, and
  - buoyancy force $\left(< 0.1 \cdot F_{drag}\right)$.
- In order of influence, the following modifications improve the results for the catching efficiency:
  1. droplet size distributions (as opposed to mono-disperse droplet distributions),
  2. splashing,
  3. droplet deformation, and
  4. rebound.
- Ice accretion thickness is matched fairly well by the numerical method;
  - micro-features (i.e., feathers or ridges) are under predicted,
  - in 3D micro-features are less accurately predicted than in 2D.

- The limits of ice accretions on airfoils and wings are in line with experimental results.

The most significant deviation of numerical results compared to experimental results lies in the under prediction of the micro-features. A significant time-dependent effect is present in the micro-features. When a small amount of ice accretes on the airfoil or wing surface this influences the flow. A new, additional, stagnation point is formed on the micro-feature, causing more ice to be accreted onto this micro-feature; causing it to grow. The current study has not analyzed the effect or the possibility of splitting the ice accretion simulation into multiple subsequent time steps.

In general the following can be said about the results for the catching efficiency and the ice accretion shape:

- The catching efficiency calculated by the numerical method is within approximately 10%.
- The ice accretion shape calculated by the numerical model is within approximately 10% when considering the maximum accretion thickness.
- The results for 3D flow are slightly less accurate than the results for 2D flow.

8.2 RECOMMENDATIONS

Related to the above conclusions, these are the recommendations for further research:

- Results show an inability of the computational method to accurately capture the catching efficiency around the leading edge. It is suspected that this is caused by secondary (splashed/rebounded) droplets re-impinging on or near the leading edge. The number and mass of re-impinging droplets may be over-predicted by the present computational model because of missing breakup effects on secondary droplets or a lack of resolution in droplet diameter.
- Prediction of micro-features in the calculated ice accretions is very difficult. These features exist because of flow patterns changing in

time, something which has not been investigated in this thesis. This may be expanded by adding a time influence in either one of two flow solutions: the surrounding fluid (air) flow or the liquid film flow on the airfoil surface.

- The method has been tested and validated for flow fields in the potential flow regime ($M < 0.3$). It would be relevant to include results beyond this limit into a validation study, the method is capable of using surrounding fluid flow solutions from any computational method as an input flow, i.e., higher velocity flows are within reach of the developed method.
- Further validation of the ice accretion method, especially for 3D flow is recommended. The extension to 3D flow in the present study has only been validated for a single case of truly 3D ice accretion.

TRACED RESULTS FROM PAPADAKIS ET AL. [2007]

A

In the article of Papadakis et al. [2007] the resulting catching efficiencies are only provided in the form of figures. To be able to compare numerical results with this experimental data, these figures have been traced. The resulting tables are provided here.

Table A.1: *Traced values for* 20 µm MVD *from Papadakis et al. [2007]*

s [mm]	β [−]
−198.562615704	0.00155763239875
−187.072490031	0.00155763239875
−182.763692903	0.00155763239875
−171.27356723	0.00155763239875
−152.602113011	0.00155763239875
−141.111987338	0.00155763239875
−129.621861664	0.00155763239875
−118.131735991	0.00155763239875
−110.950407445	0.00155763239875
−102.33281319	0.00155763239875
−90.8426875171	0.00155763239875
−83.6602403843	0.00311526479751
−79.3514432569	0.00311526479751
−67.8601989966	0.00467289719626
−59.2403675677	0.00778816199377
−52.7738161155	0.01246105919
−49.8990475232	0.0155763239875
−45.5857760477	0.0218068535826
−43.428021723	0.0264797507788
−40.5510159566	0.0327102803738
−37.6717730163	0.0420560747664

Table continued on next page

Table continued from previous page

s [mm]	β [−]
−35.5095443436	0.0529595015576
−32.6280642293	0.0654205607477
−29.7443469409	0.0809968847352
−27.5754067462	0.101246105919
−23.9657264943	0.127725856698
−21.070823336	0.158878504673
−18.8951716192	0.188473520249
−15.9980312869	0.222741433022
−13.0941794325	0.266355140187
−10.9073418458	0.311526479751
−7.99901564344	0.361370716511
−5.80770370868	0.41277258567
−2.16894019475	0.479750778816
0.0246089140198	0.534267912773
2.19690486977	0.559190031153
5.06048759207	0.546728971963
7.90169857436	0.503115264798
10.7294865126	0.440809968847
13.5595116249	0.381619937695
15.6747596436	0.327102803738
18.5103776909	0.275700934579
21.3493514992	0.228971962617
24.1927996555	0.188473520249
26.3237078922	0.155763239875
29.1716303965	0.121495327103
32.0262644228	0.0965732087227
34.8864913841	0.0794392523364
37.0297040778	0.0638629283489
38.459258265	0.0545171339564
42.0420924288	0.0436137071651
44.9101494992	0.0373831775701
47.7782065695	0.0311526479751
50.6462636398	0.0249221183801
53.5187950581	0.0249221183801

Table continued on next page

Table continued from previous page

s [mm]	β [−]
55.6720750348	0.0233644859813
57.8253550115	0.0218068535826
60.6956492559	0.018691588785
63.5681806742	0.018691588785
66.4407120925	0.018691588785
68.5939920692	0.0171339563863
71.4665234875	0.0171339563863
78.6456148593	0.0140186915888
85.1076919635	0.01246105919
93.0060347769	0.0109034267913
106.649440427	0.00934579439252
120.292846077	0.00778816199377
136.808783145	0.00623052959502
151.888454504	0.00467289719626
174.149454409	0.00311526479751
187.075845792	0.00311526479751
189.949495797	0.00467289719626

Table A.2: *Traced values for* 236 µm MVD *from Papadakis et al. [2007]*

s [mm]	β [−]
−198.077634011	0.0016051364366
−193.271719039	0.0000000000000
−182.6987061	0.0016051364366
−177.892791128	0.00321027287319
−171.164510166	0.0016051364366
−161.552680222	0.0016051364366
−150.979667283	0.0000000000000
−145.212569316	0.0000000000000
−132.717190388	0.0016051364366
−125.988909427	0.00321027287319
−118.299445471	0.00642054574639
−110.609981516	0.0128410914928
−103.881700555	0.0208667736758

Table continued on next page

Table continued from previous page

s [mm]	β [−]
−100.036968577	0.024077046549
−98.1146025878	0.0272873194222
−93.3086876155	0.0321027287319
−91.3863216266	0.0353130016051
−88.5027726433	0.0529695024077
−85.6192236599	0.0642054574639
−81.7744916821	0.0674157303371
−79.8521256932	0.0706260032103
−76.9685767098	0.0786516853933
−75.0462107209	0.091492776886
−72.1626617375	0.099518459069
−69.2791127542	0.110754414125
−66.3955637708	0.126805778491
−63.5120147874	0.142857142857
−60.6284658041	0.154093097913
−58.7060998152	0.163723916533
−55.8225508318	0.181380417335
−53.9001848429	0.197431781701
−51.0166358595	0.211878009631
−48.1330868762	0.22632423756
−45.2495378928	0.24077046549
−43.3271719039	0.266452648475
−40.4436229205	0.284109149278
−37.5600739372	0.30176565008
−34.6765249538	0.327447833066
−31.7929759704	0.351524879615
−28.9094269871	0.375601926164
−26.9870609982	0.394863563403
−25.0646950092	0.423756019262
−21.2199630314	0.449438202247
−18.3364140481	0.475120385233
−16.4140480591	0.512038523274
−13.5304990758	0.545746388443
−10.6469500924	0.598715890851

Table continued on next page

Table continued from previous page

s [mm]	β [−]
−7.76340110906	0.68378812199
−4.87985212569	0.772070626003
−2.95748613678	0.865168539326
−0.0739371534196	0.937399678973
1.84842883549	0.950240770465
4.73197781885	0.903691813804
7.61552680222	0.807383627608
10.4990757856	0.69341894061
13.3826247689	0.585874799358
15.3049907579	0.512038523274
18.1885397412	0.459069020867
21.0720887246	0.412520064205
23.9556377079	0.372391653291
25.8780036969	0.333868378812
29.7227356747	0.30176565008
32.606284658	0.271268057785
34.528650647	0.248796147673
36.4510166359	0.229534510433
40.2957486137	0.210272873194
42.2181146026	0.192616372392
45.101663586	0.178170144462
47.0240295749	0.162118780096
49.9075785582	0.157303370787
52.7911275416	0.14606741573
55.674676525	0.131621187801
58.5582255083	0.133226324238
60.4805914972	0.126805778491
62.4029574861	0.120385232745
66.247689464	0.120385232745
70.0924214418	0.113964686998
71.0536044362	0.112359550562
73.9371534196	0.117174959872
77.7818853974	0.117174959872
80.6654343808	0.109149277689

Table continued on next page

Table continued from previous page

s [mm]	β [−]
83.5489833641	0.104333868379
84.5101663586	0.102728731942
89.3160813309	0.107544141252
91.2384473198	0.107544141252
95.0831792976	0.0979133226324
98.9279112754	0.0947030497592
101.811460259	0.0930979133226
106.617375231	0.0979133226324
110.462107209	0.0947030497592
115.268022181	0.0930979133226
121.035120148	0.0898876404494
123.918669131	0.0850722311396
127.763401109	0.0850722311396
132.569316081	0.0866773675762
137.375231054	0.0818619582665
142.181146026	0.0770465489567
144.103512015	0.0770465489567
148.909426987	0.0722311396469
150.831792976	0.0690208667737
154.676524954	0.0690208667737
156.598890943	0.0690208667737
160.443622921	0.0690208667737
163.327171904	0.0674157303371
168.133086876	0.0626003210273
170.055452865	0.0593900481541
172.939001848	0.0593900481541
175.822550832	0.0529695024077
178.706099815	0.0497592295345
181.589648799	0.0545746388443
184.473197782	0.0529695024077
190.240295749	0.0561797752809
192.162661738	0.0513643659711
196.96857671	0.0513643659711
198.890942699	0.0481540930979

Table continued on next page

Table continued from previous page

s [mm]	β [−]
202.735674677	0.0449438202247
210.425138632	0.0385232744783
220.036968577	0.0321027287319
226.765249538	0.0272873194222
231.57116451	0.0256821829856
235.415896488	0.0256821829856
243.105360444	0.0256821829856
249.833641405	0.0208667736758
257.52310536	0.0192616372392
265.212569316	0.0176565008026
270.018484288	0.016051364366
278.669131238	0.0128410914928
285.3974122	0.0112359550562
291.164510166	0.0112359550562
300.776340111	0.00802568218299
303.659889094	0.00642054574639
311.34935305	0.00642054574639
316.155268022	0.00481540930979
316.155268022	0.00481540930979

BIBLIOGRAPHY

C. Bai and A.D. Gosman. Development of methodology for spray impingement simulation. Technical Report 950283, SAE, 400 Commonwealth Drive, Warrendale, PA, 1995. 36

G.E. Cossali, A. Coghe, and M. Marengo. The impact of a single drop on a wetted solid surface. *Experiments in Fluids*, 22(6):463–472, April 1997. 31

M. De Gennaro. A. feo droplet drag model. Email communication, Februari 2009. University of Naples "Federico II". 26

Jeroen E. Dillingh and H.W.M. Hoeijmakers. Simulation of ice accretion on airfoils during flight. In *FAA In-Flight Icing/Ground De-Icing International Conference & Exhibition*, Chicago, IL, June 2003. 12 pages. 11

Jeroen E. Dillingh and H.W.M. Hoeijmakers. Numerical simulation of airfoil ice accretion and thermal anti-icing systems. In *ICAS 2004*, 24th international congress of the aeronautical sciences, Yokohama, Japan, August-September 2004. 11

A. Feo and E. Jarillo. Preliminary sld measurements for drag coefficient determination. INTA internal technical report, AE/TNO/4420/281/INTA/08, July 2008. 26, 67

R. Honsek, W.G. Habashi, and M.S. Aubé. Eulerian modeling of in-flight icing due to supercooled large droplets. *Journal of Aircraft*, 45(4):1290–1296, July-August 2008. 27, 35, 36

J.M. Hospers. Development and application of hybrid grids for finite volume methods. Master's thesis, University of Twente, Enschede, the Netherlands, December 2007. 79

Sander J. Jacobs, Jacco M. Hospers, and H.W.M. Hoeijmakers. Numerical simulation of ice accretion on multiple-element airfoil sections. In *ICAS*

2008, 26th international congress of the aeronautical sciences, Anchorage, AK, September 2008. 11

Philip H. Kelleners. *An edge-based finite volume method for inviscid compressible flow with condensation.* PhD thesis, University of Twente, Enschede, the Netherlands, December 2007. 40

Arjen H. Koop. *Numerical simulation of unsteady three-dimensional sheet cavitation.* PhD thesis, University of Twente, Enschede, the Netherlands, September 2008. 40

I. Langmuir and K.B. Blodgett. A mathematical investigation of water droplet trajectories. Technical Report 5418, US Army Air Forces, 1946. 12, 39

R. Mei, C.J. Lawrence, and R.J. Adrian. Unsteady drag on a sphere at finite reynolds-number with small fluctuations in the free-stream velocity. *Journal of Fluid Mechanics*, 233:613–631, 1991. 22

Bernard L. Messinger. Equilibrium temperature of an unheated icing surface as a function of air speed. *Journal of Aeronautical Sciences*, 20(1):29–42, January 1953. 13

G. Mingione. EXTICE. final report, FP7-AT-2007-RTD-1-211927, May 2012. 26

C. Mundo, M. Sommerfeld, and C. Tropea. Droplet-wall collisions: experimental studies of the deformation and breakup process. *International Journal of Multiphase Flow*, 21(2):151–173, 1995. 32

E. Norde. Splashing model for impact of supercooled large droplets on a thin liquid film. Master's thesis, University of Twente, Enschede, the Netherlands, February 2013. 20, 89

Peter J. O'Rourke and Anthony A. Amsden. The tab method for numerical calculation of spray droplet breakup. In *International Fuels and Lubricants Meeting and Exposition*, Toronto, Canada, 1987. 29

Michael Papadakis, Arief Rachman, See-Cheuk Wong, Hsiung-Wei Yeong, Kuohsing E. Hung, Giao T. Vu, and Colin S. Bidwell. Water droplet

impingement on simulated glaze, mixed and rime ice accretions. Technical Report NASA/TM-213961, NASA, National Technical Information Service, 5285 Port Royal Road, Springfield, VA 22100, October 2007. 23, 57, 58, 59, 87, 107

M. Pilch and C.A. Erdman. Use of breakup time data and velocity history data to predict the maximum size of stable fragments for acceleration-induced breakup of a liquid drop. *International Journal of Mulitphase Flow*, 13(6):741–757, 1987. 27, 28, 29

M. Snellen. Ice accretion during flight. memorandum m-749. Technical report, Department of Aerospace Engineering, Delft University of Technology, Delft, The Netherlands, 1996. 11

M. Snellen, O.J. Boelens, and H.W.M. Hoeijmakers. A computational method for numerically simulating ice accretion. In *15th AIAA Applied Aerodynamics Conference*, number 15, Atlanta, GA, June 1997. AIAA. Technical Papers pt 2. 11

C.D. Stow and M.G. Hadfield. An experimental investigation of fluid flow resulting from the impact of a water drop with an unyielding dry surface. *Proceedings of the Royal Society Londen A*, 373:419–441, 1981. 32

C.D. Stow and R.D. Stainer. The physical products of a splashing water drop. *Journal of the Meteorological Society of Japan*, 55(5):518–532, 1977. 33

J. Tan, M. Papadakis, and M.K. Sampath. Computational study of large droplet breakup in the vicinity of an airfoil. Technical report, U.S. Department of Transportation, Federal Aviation Administration, Office of Aviation Research, Washingtion, DC 20591, U.S.A, October 2005. 26, 27

M.F. Trujillo, W.S. Mathews, C.F. Lee, and J.F. Peters. Modelling and experiment of impingement and atomization of a liquid spray on a wall. *International Journal of Engine Research*, 1(1):87–105, 2000. ISSN 1468-0874. 32

Dirk F. van Eijkeren and H.W.M. Hoeijmakers. Influence of the history term in a lagrangian method for oil-water separation. In *7th International Conference on Multiphase Flow*, Tampa, FL, 2010. 20

Giao T. Vu, Hsiung Wei Yeong, Colin S. Bidwell, Marlin D. Breer, and Timothy J. Bencic. Experimental investigation of water droplet impingement on airfoils, finite wings, and an s-duct engine inlet. Technical Report NASA/TM-211700, NASA, National Technical Information Service, 5285 Port Royal Road, Springfield, VA 22100, October 2002. 58, 60, 71

W.B. Wright and M.G. Potapczuk. Semi-empirical modelling of sld physics. In *42nd AIAA Aerospace Sciences Meeting and Exhibit*, Reno, NV, January 2004. 20

A.L. Yarin and D.A. Weiss. Impact of drops on solid surfaces: self-similar capilary waves, and splashing as a new type of kinematic discontinuity. *Journal of Fluid Mechanics*, 283:141–173, January 1995. 32

ABOUT THE AUTHOR

Jacco Hospers was born in Almelo on the 25th of October 1983. After a short stint in the army, he joined the Mechanical Engineering program of the University of Twente in 2002. In 2007 he earned his Masters of Science degree in the field of computational fluid dynamics in the Engineering Fluid Dynamics group of professor Hoeijmakers. After graduation he was invited to become part of the EXTICE program in pursuit of a doctorate culminating in he work you have before you now.

During this period the following scientific work has been produced:

J.M. Hospers. Development and application of hybrid grids for finite volume methods. Master's thesis, University of Twente, Enschede, the Netherlands, December 2007. 79

Sander J. Jacobs, Jacco M. Hospers, and H.W.M. Hoeijmakers. Numerical simulation of ice accretion on multiple-element airfoil sections. In *ICAS 2008*, 26th international congress of the aeronautical sciences, Anchorage, AK, September 2008. 11

J.M. Hospers and H.W.M. Hoeijmakers. Numerical prediction of SLD ice accretion on multi-element airfoils. In *48th Aerospace Sciences Meeting*, Orlando, FL, January 2010a.

J.M. Hospers and H.W.M. Hoeijmakers. Numerical prediction of SLD ice accretion on multi-element airfoils. In *7th International Conference on Multiphase Flow*, Tampa, FL, May 2010b.

J.M. Hospers and H.W.M. Hoeijmakers. Numerical simulation of SLD ice accretion. In *27th International Congress of the Aeronautical Sciences, ICAS 2010*, Nice, France, September 2010c.

J.M. Hospers and H.W.M. Hoeijmakers. Numerical simulation of SLD ice accretion. In *SAE 2011 International Conference on Aircraft and Engine Icing and Ground Deicing*, Chicago, IL, June 2011.

J.M. Hospers and H.W.M. Hoeijmakers. Eulerian method for the simulation of 3D ice accretions. Presentation at Burgersdag 2012, JMBC, Eindhoven, the Netherlands, January 2012.